Remote Sensing of Environment 235 (2019) 111491

Contents lists available at ScienceDirect

Remote Sensing of Environment

journal homepage: www.elsevier.com/locate/rse

An empirical algorithm to seamlessly retrieve the concentration of suspended particulate matter from water color across ocean to turbid river mouths

Xiaolong Yu[a,b,c,*], Zhongping Lee[a], Fang Shen[c], Menghua Wang[d], Jianwei Wei[d], Lide Jiang[d], Zhehai Shang[a]

[a] University of Massachusetts Boston, School for the Environment, Boston, MA, 02125, USA
[b] State Key Laboratory of Marine Environmental Science, College of Ocean and Earth Sciences, Xiamen University, Xiamen, 361101, China
[c] State Key Laboratory of Estuarine and Coastal Research, East China Normal University, Shanghai, 200062, China
[d] NOAA National Environmental Satellite, Data, and Information Service, Center for Satellite Applications and Research, E/RA3, 5830 University Research Court, College Park, MD, 20740, USA

ARTICLE INFO

Keywords:
Remote sensing reflectance
Suspended particulate matter
Water color
VIIRS
Turbid waters
Global algorithm

ABSTRACT

We propose a globally applicable algorithm (GAA_{SPM}) to seamlessly retrieve the concentration of suspended particulate matter (SPM) (C_{SPM}) from remote sensing reflectance ($R_{rs}(\lambda)$) across ocean to turbid river mouths without any hard-switching in its application. GAA_{SPM} is based on a calibrated relationship between C_{SPM} and a generalized index for SPM (GI_{SPM}) from water color. The GI_{SPM} is mainly composed of three $R_{rs}(\lambda)$ ratios (671, 745, and 862 nm over 551 nm, respectively), along with weighting factors assigned to each ratio. The weighting factors are introduced to ensure the progressive application of $R_{rs}(\lambda)$ in the longer wavelengths for increasing C_{SPM}. Calibration of GAA_{SPM} employed data collected from multiple estuarine and coastal regions of Europe, China, Argentina, and the USA with the measured C_{SPM} spanning from 0.2 to 2068.8 mg/L. Inter-comparison with several recalibrated well-known C_{SPM} retrieval algorithms demonstrates that GAA_{SPM} has the best retrieval accuracy over the entire C_{SPM} range with a relative mean absolute difference (rMAD) of 41.3% (N = 437). This averaged uncertainty in GAA_{SPM}-derived C_{SPM} is mostly attributed to the retrievals from less turbid waters where $C_{SPM} < 50$ mg/L (rMAD = 50%, N = 214). GAA_{SPM} was further applied to the Visible Infrared Imaging Radiometer Suite (VIIRS) measurements over prominent coastal areas and produced reliable C_{SPM} maps along with realistic spatial patterns. In contrast, applications of other C_{SPM} algorithms resulted in less reliable C_{SPM} maps with either unjustified numerical discontinuities in the C_{SPM} spatial distribution or unsatisfactory retrieval accuracy. Therefore, we propose GAA_{SPM} as a preferred algorithm to retrieve C_{SPM} over regions with a wide range of C_{SPM}, such as river plume areas.

1. Introduction

Suspended particulate matter (SPM) is one of the important water constituents that determines water clarity. Knowledge of SPM dynamics in the estuarine and coastal waters could advance our understanding of erosion and deposition processes, biomass primary production, and the transport of sediments, nutrients, and heavy metals (Volpe et al., 2011). Quantitative and accurate monitoring of the SPM dynamics has, therefore, long been desired for effective coastal management and water quality assessment (Nechad et al., 2010). Traditional methods with discrete sampling can only provide limited information on the spatial-temporal variation of SPM. The remote sensing technique, on the other hand, can provide frequent, synoptic, and consistent observations (IOCCG, 2000, 2006).

Because the concentration of SPM (C_{SPM}, in mg/L) can alter the appearance of water color, there has been a long history of retrieving C_{SPM} from ocean color, such as the remote sensing reflectance ($R_{rs}(\lambda)$, in sr^{-1}). Generally, $R_{rs}(\lambda)$ is a function of the total absorption and backscattering coefficients ($a(\lambda)$ and $b_b(\lambda)$, respectively), and $a(\lambda)$ and $b_b(\lambda)$ are functions of C_{SPM}. In extremely clear waters, particularly the ocean gyres, the extremely low concentrations of suspended inorganic matter delivered from the air and the suspended organic matter, such as phytoplankton detritus, do not contribute much to either $a(\lambda)$ or $b_b(\lambda)$, resulting in a less sensitive correlation between $R_{rs}(\lambda)$ and C_{SPM}. The

* Corresponding author. University of Massachusetts Boston, School for the Environment, Boston, MA, 02125, USA.
E-mail address: xiaolong.yu@umb.edu (X. Yu).

https://doi.org/10.1016/j.rse.2019.111491
Received 6 March 2019; Received in revised form 13 October 2019; Accepted 20 October 2019
Available online 25 October 2019
0034-4257/ © 2019 Elsevier Inc. All rights reserved.

relatively large uncertainties of the measured $R_{rs}(\lambda)$ and C_{SPM} in such waters could also contribute to the poor $R_{rs}(\lambda)$-C_{SPM} correlation. With increasing C_{SPM}, $R_{rs}(\lambda)$ starts to be sensitive to C_{SPM}, especially at visible bands (VIS) (Binding et al., 2005; Loisel et al., 2014). However, $R_{rs}(\lambda)$ in the visible bands tend to saturate and the C_{SPM}-sensitive wavelength shifts to longer wavelength at the near-infrared (NIR) bands in turbid waters (Luo et al., 2018; Shen et al., 2010a) and even to the shortwave infrared (SWIR) bands in extremely turbid waters (Knaeps et al., 2015; Nechad et al., 2010; Shi et al., 2018). As a result, C_{SPM} was preferably retrieved from $R_{rs}(\lambda)$ at the NIR and SWIR bands for highly turbid waters (Doxaran et al., 2002a, 2002b; 2003; He et al., 2013; Zhang et al., 2010).

However, existing algorithms were mostly developed for a specific range of C_{SPM} and are not suitable for general applications in turbid estuarine and coastal waters, where C_{SPM} could span over four orders of magnitude. Alternative methods were proposed with multiple algorithms employed for different C_{SPM} ranges associated with hard-wired switching schemes (Shen et al., 2010b, 2014). But using hard-wired switching schemes always come with a demerit that the derived C_{SPM} will likely result in discontinuity, which is particularly apparent when applying such schemes to satellite data (Shen et al., 2013). Switching algorithms employing a blending scheme were also proposed to ensure a smooth transition between algorithm output (Dogliotti et al., 2015; Han et al., 2016; Novoa et al., 2017). However, these algorithms require reflectance values at certain wavelengths as the switching boundaries, which differed significantly in the published studies. It is, thus, a challenge to choose the 'right' boundaries for global applications. Therefore, novel and mechanistic algorithms that can obtain smooth and natural coverage of C_{SPM} in coastal regions are still strongly desired.

In this study, we propose a globally applicable algorithm for C_{SPM} retrieval (GAA_{SPM}) to account for the shifting of the most sensitive $R_{rs}(\lambda)$ to increasing C_{SPM}. Calibration of GAA_{SPM} was conducted by *in situ* data collected from multiple estuarine and coastal regions around the world, resulting in reliable C_{SPM} retrievals for both clear and turbid waters. Further, GAA_{SPM} was applied to the Visible Infrared Imaging Radiometer Suite (VIIRS) images and produced reasonable C_{SPM} maps over turbid estuarine and coastal waters along with realistic spatial patterns.

2. Data and methods

2.1. In situ datasets

Four *in situ* datasets with simultaneous measurements of C_{SPM} and $R_{rs}(\lambda)$ were employed in this study for algorithm calibration and validation. The four datasets consist of the Changjiang, the SeaSWIR, the University of Massachusetts Boston (UMB), and the Coastal Surveillance through Observation of Ocean Color (COASTLOOC) datasets, with the locations of sampling sites presented in Fig. 1.

2.1.1. The Changjiang dataset

Three field campaigns were conducted in the Changjiang (Yangtze River, China) estuary in February and June of 2011 and March of 2013. $R_{rs}(\lambda)$ spectra were measured by the Hyperspectral Surface Acquisition System (HyperSAS, Satlantic Inc., Canada), which concurrently measures the upwelling radiance above the sea surface ($L_t(\lambda)$, in $W/m^2/nm/sr$), the sky radiance ($L_i(\lambda)$, in $W/m^2/nm/sr$), and the downwelling irradiance just above the surface ($E_s(\lambda)$, in $W/m^2/nm$) from 350 to 858 nm in 136 spectral channels. The viewing geometry of the mounted sensors was conformed to the NASA protocol to minimize sun glint contamination (Fargion and Mueller, 2000). $R_{rs}(\lambda)$ was calculated from the radiometric measurements following (Mobley, 1999),

$$R_{rs}(\lambda) = \frac{L_w(\lambda)}{E_s(\lambda)} = \frac{L_t(\lambda) - \rho L_i(\lambda)}{E_s(\lambda)} \quad (1)$$

where ρ is the sea-surface reflectance factor, which is a function of solar zenith angle and surface roughness and is computed by the Ruddick-Hojerslev model (Ruddick et al., 2006). The spectra of obtained $R_{rs}(\lambda)$ are presented in Fig. 2a.

Water samples were collected in duplicates concurrently with radiometric measurements at each station and then filtered on board using pre-combusted (450 °C for 6 h) and pre-weighed GF/F glass microfiber filters (Whatman ®). Particle-loaded filters were rinsed three times with Milli-Q water to remove dissolved salt and temporarily stored in a −20 °C freezer during the cruise. The filters were dried at 60 °C for 24 h and then re-weighed in the laboratory. SPM concentration of each sample was calculated as the difference between the re-weighed particle-loaded filter and the pre-weighed blank filter and then divided by the volume of filtered water. C_{SPM} of each station was averaged from the duplicate measurements, which varied from 0.7 mg/L to 2068.8 mg/L with a mean value of 412.4 mg/L. Table 1 summarizes the four datasets with a brief description of each dataset.

2.1.2. The SeaSWIR dataset

The SeaSWIR dataset is a publicly available dataset, which consists of 137 concurrent measurements of $R_{rs}(\lambda)$ and C_{SPM} at three turbid estuarine sites in the Gironde of France, the Río de La Plata of Argentina, and the Scheldt of Belgium (Knaeps et al., 2018). $R_{rs}(\lambda)$ spectra were measured by ASD (Analytical Spectral Devices, Inc.) with a spectral resolution of 1 nm from 350 to 2500 nm. The SeaSWIR dataset provides only $R_{rs}(\lambda)$ from 350 to 1300 nm because water is black beyond 1300 nm. Fig. 2b presents the $R_{rs}(\lambda)$ spectra of the SeaSWIR data from 400 to 900 nm. SPM samples were also filtered using the GF/F filters with the measured C_{SPM} ranging from 48.3 to 1400.5 mg/L and a mean value of 275.1 mg/L. Details regarding the measurements of $R_{rs}(\lambda)$ and C_{SPM} are described in Knaeps et al. (2018).

2.1.3. The UMB dataset

The UMB dataset includes data collected from one cruise in the Gulf of Mexico in September 2013 and four cruises in the Massachusetts Bay from June to November of 2018. $R_{rs}(\lambda)$ spectra were measured by a floating system, named the Radiometer Incorporated Skylight Blocked Apparatus (RISBA) (Lee et al., 2013). This RISBA is equipped with one hyperspectral irradiance sensor and one radiance sensor (HyperOCI, Satlantic Inc.) with radiometric measurements at ~3 nm increments from 350 to 800 nm. The radiance sensor, incorporated with a custom designed cone, can measure spectral water-leaving radiance ($L_w(\lambda)$) directly by blocking off the surface-reflected skylight. With simultaneously measured $E_s(\lambda)$ by the irradiance sensor, $R_{rs}(\lambda)$ can be computed as the ratio of $L_w(\lambda)$ and $E_s(\lambda)$. The computed $R_{rs}(\lambda)$ was later corrected for the instrument self-shadowing (Shang et al., 2017). Note that RISBA was always kept > 20 m away from the ship to minimize ship perturbations during the deployment. The uncertainties of measured $R_{rs}(\lambda)$ by RISBA are around 5% in visible bands (Lee et al., 2013). The spectra of measured $R_{rs}(\lambda)$ are presented in Fig. 2c. Determination of SPM concentration adopted the same method as described in Section 2.1.1, with the measured C_{SPM} ranging from 0.2 to 30.6 mg/L and averaged at 5.7 mg/L.

2.1.4. The COASTLOOC dataset

The COASTLOOC dataset consists of 422 observations of marine reflectance and bio-optical parameters collected from European coastal waters (Babin et al., 2003). It was the irradiance reflectance just beneath the sea surface $R(\lambda, 0^-)$ available in the COASTLOOC dataset instead of $R_{rs}(\lambda)$. The raw COASTLOOC dataset was filtered for concurrent measurements of C_{SPM} and $R(\lambda, 0^-)$ at 411, 443, 456, 490, 509, 532, 619, 665, 683, 705, 779, and 866 nm, where 99 observations were retained. SPM samples were also filtered using the GF/F filters with the measured C_{SPM} ranging from 0.7 to 72.8 mg/L and averaged at 4.8 mg/L. The $R(\lambda, 0^-)$ was converted to $R_{rs}(\lambda)$ based on Zhang and Fell (2007),

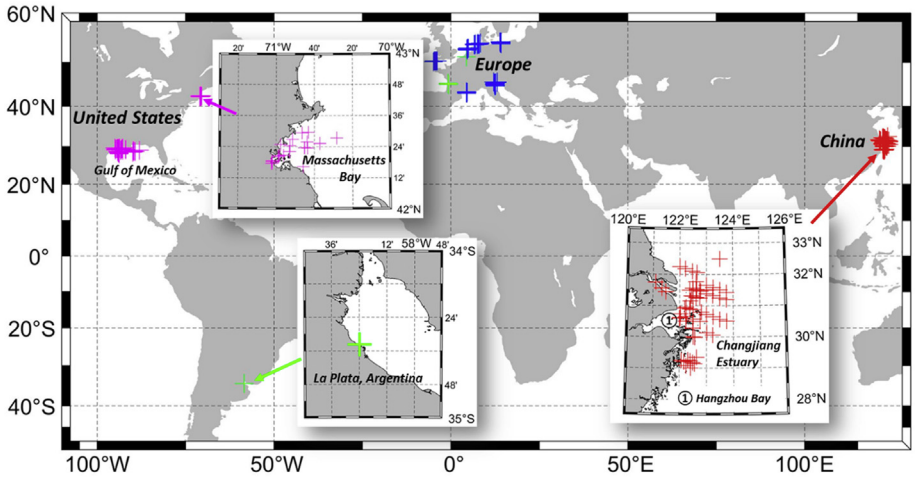

Fig. 1. Sampling locations of the four *in situ* datasets. The red, green, magenta, and blue crosses represent the Changjiang, the SeaSWIR, the UMB, and the COASTLOOC datasets, respectively. Three insert figures zoom in the sampling locations in the Massachusetts Bay, the Río de La Plata estuary, and the Changjiang estuary, respectively. (For interpretation of the references to color in this figure legend, the reader is referred to the Web version of this article.)

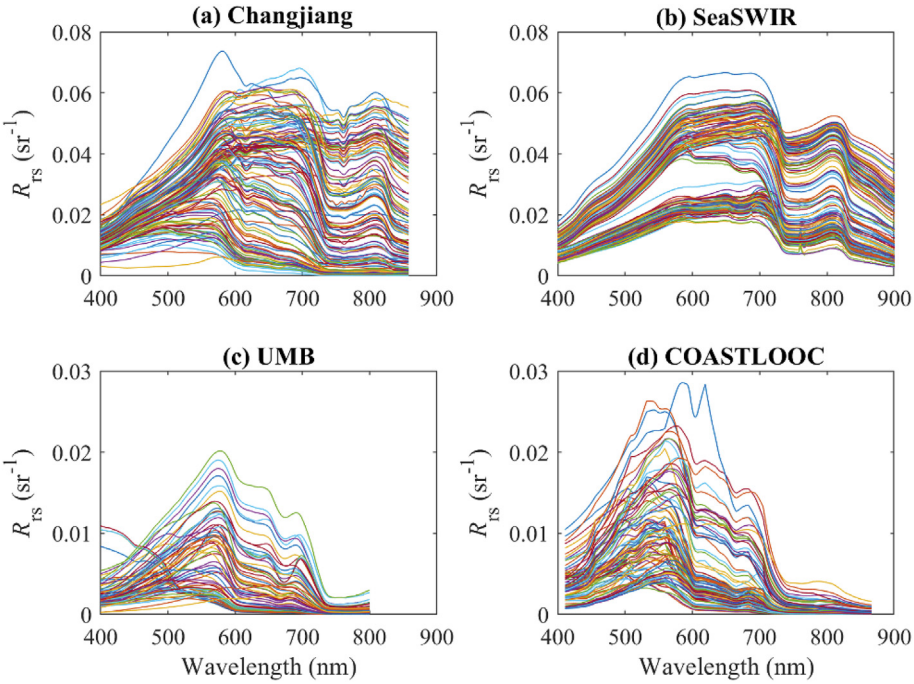

Fig. 2. Measured $R_{rs}(\lambda)$ spectra of the Changjiang (a), the SeaSWIR (b), the UMB (c), and the COASTLOOC (d) datasets.

$$R_{rs}(\lambda) = \frac{1}{Q}\frac{t^2}{n^2}R(\lambda,\ 0^-) \quad (2)$$

where t is the transmittance of the air-sea interface, n is the real part of the complex refraction index of seawater, and Q is the upwelling irradiance-to-radiance ratio. In this study, t^2/n^2 is approximated by a constant factor of 0.54 (Austin, 1974) and Q is set to 4.0 (Loisel and Morel, 2001), resulting in $R_{rs}(\lambda) = 0.133\,R(\lambda, 0^-)$. Note that Q typically varies between 3.5 and 5.0 under typical measurement conditions (Loisel and Morel, 2001). A simplified solution to Eq. (2) with constant Q will introduce uncertainties to calculated $R_{rs}(\lambda)$. However, the dependencies of Q could be mostly canceled out when $R_{rs}(\lambda)$ ratios are used for algorithm development (Zhang and Fell, 2007).

Since $R_{rs}(745)$ is required in this study for algorithm development, while this wavelength is absent from the COASTLOOC dataset, the multispectral $R_{rs}(\lambda)$ was interpolated to hyperspectral $R_{rs}(\lambda)$ using a semi-analytic approach (described in Appendix 1). The spectral $R_{rs}(\lambda)$ of the retained COASTLOOC observations are shown in Fig. 2d. Note that uncertainties of the interpolated $R_{rs}(745)$ could have minimal impacts on the derived C_{SPM} for the COASTLOOC dataset as C_{SPM} is generally low in this dataset (see discussions in Section 4.2).

2.2. VIIRS and atmospheric correction

VIIRS, onboard the Suomi National Polar-orbiting Partnership (SNPP) satellite, is one of the operational moderate resolution ocean color imagers with a spatial resolution of 750 m. VIIRS-SNPP acquires radiometric measurements at seven spectral bands from the visible to NIR, with the nominal center wavelengths of 410, 443, 486, 551, 671, 745, and 862 nm. In this study, VIIRS images were atmospherically corrected by the NOAA Multi-Sensor Level-1 to Level-2 (MSL12) ocean color data processing system using a combined NIR and SWIR atmospheric correction algorithm (Wang, 2007; Wang and Shi, 2007). The NIR-SWIR algorithm proceeds with the standard NIR algorithm for the open oceans (Gordon and Wang, 1994), whereas the SWIR algorithm is used for the turbid waters in coastal regions (Wang, 2007; Wang and Shi, 2007). The NIR algorithm assumes 'black ocean' at the NIR bands (745 and 862 nm), while the SWIR algorithm adjusts the assumption to the SWIR bands (1238 and 1601 nm) for turbid waters (Jiang and

Table 1
Brief descriptions and overview of the four *in situ* datasets collected from multiple estuarine and coastal areas.

Datasets	SPM range (Mean) (mg/L)	R_{rs} Spectral range (nm)	No.	Instrument	Sampling Dates	Sampling Regions
Changjiang	0.7–2068.8 (412.4)	350–858	130	HyperSAS	Feb, Jun 2011, Mar 2013	Changjiang River and Estuary
SeaSWIR	48.3–1400.5 (275.1)	350–1300	137	ASD	Oct 2010–Aug 2013	Scheldt River, Gironde River, Río de La Plata
UMB	0.2–30.6 (5.7)	350–800	71	RISBA	Sep 2013, Jun–Nov 2018	Gulf of Mexico, Massachusetts Bay
COASTLOOC	0.7–72.8 (4.8)	411, 443, 456, 490, 509, 532, 619, 665, 683, 705, 779, 866	99	NA[a]	Apr 1997–Sep 1998	European coastal waters

[a] NA indicates no information available or not applicable.

Wang, 2014). A turbid water index, developed by Shi and Wang (2007), is pre-computed to identify the turbid water pixels where the SWIR algorithm can be implemented.

To evaluate the performance of VIIRS $R_{rs}(\lambda)$ products, satellite match-up pairs were acquired over a 3-by-3-pixel window centered at the *in situ* sampling site with the following criteria applied. First, the field-measured $R_{rs}(\lambda)$ were sampled within 1 h of the VIIRS-SNPP overpass. The selected time difference is to account for the significant spatial-temporal variabilities of water masses in estuarine and coastal waters due to the strong tide and rapid current and runoff. Second, at least 50% of the pixels were valid within the 3-by-3-pixel window. All pixels flagged as land, cloud, cloud straylight or shadow contamination, high glint, and atmospheric correction failure were considered invalid. For the SeaSWIR dataset, this threshold was relaxed to 30% because some of the sampling sites were dock-based, and at least one-third of the 3-by-3-pixel window is flagged as land. At last, the median $R_{rs}(\lambda)$ of the 3-by-3-pixel window was used as satellite-derived $R_{rs}(\lambda)$.

2.3. Algorithms for C_{SPM} retrievals

The Changjiang and UMB datasets do not have $R_{rs}(862)$ that required for algorithm development. For the Changjiang dataset, which has comparable C_{SPM} range with the SeaSWIR dataset (Table 1), $R_{rs}(862)$ is computed from measured $R_{rs}(858)$ using the $R_{rs}(862)$-$R_{rs}(858)$ relationship calibrated from the SeaSWIR dataset ($R^2 = 1$, N = 137),

$$R_{rs}(862) = 0.983 \times R_{rs}(858). \quad (3)$$

For the UMB dataset, which has similar C_{SPM} range as the COASTLOOC dataset (Table 1), $R_{rs}(862)$ is computed from measured $R_{rs}(800)$ using a calibrated relationship between interpolated $R_{rs}(800)$ and $R_{rs}(862)$ from the COASTLOOC dataset ($R^2 = 0.96$, N = 98),

$$R_{rs}(862) = 0.483 \times R_{rs}(800). \quad (4)$$

The empirical relationship of Eq. (4) could introduce extra errors to the calculated $R_{rs}(862)$. However, these errors should have minimal impacts on the derived C_{SPM} for the UMB dataset due to the low C_{SPM} values, as discussed in Section 4.2.

2.3.1. Development of a novel algorithm for wide-range C_{SPM}

C_{SPM} and $R_{rs}(\lambda)$ data pairs were partitioned into four subsets to evaluate the sensitivity of $R_{rs}(\lambda)$ to separate C_{SPM} ranges. The four groups are defined by the C_{SPM} range and are classified as 'clear' waters ($C_{SPM} < 1$ mg/L, N = 47), 'low turbidity' waters ($1 < C_{SPM} < 10$ mg/L, N = 132), 'moderate turbidity' waters ($10 < C_{SPM} < 50$ mg/L, N = 41), and 'high turbidity' waters ($C_{SPM} > 50$ mg/L, N = 217), respectively. Note that the selection of such criteria is somewhat arbitrary but can adequately demonstrate the sensitivity of $R_{rs}(\lambda)$ to increasing C_{SPM}.

The coefficient of determination (R^2) from linear regressions between C_{SPM} and $R_{rs}(\lambda)$ at a single VIIRS band and the band ratio of $R_{rs}(\lambda)$ over $R_{rs}(551)$ for the four subsets are shown in Fig. 3. As presented in Fig. 3a, the most sensitive $R_{rs}(\lambda)$ to C_{SPM} shifts progressively from 671 nm to 862 nm with increasing C_{SPM}, which is consistent with the results in Shen et al. (2010b). It is worthy to note that the ratios of $R_{rs}(\lambda)$ to $R_{rs}(551)$ have higher R^2 values with C_{SPM} than the individual $R_{rs}(\lambda)$. Therefore, C_{SPM} could be more sensitive to the band ratios, which is likely due to the fact that using band ratios can partially remove the effects of bi-directional variations of $R_{rs}(\lambda)$ (Doxaran et al., 2006). Therefore, $R_{rs}(\lambda)$ to $R_{rs}(551)$ ratios, rather than $R_{rs}(\lambda)$ values, are employed in this study to develop the retrieval algorithm for C_{SPM}.

Given that the sensitive wavelength in $R_{rs}(\lambda)$ for C_{SPM} varies with increasing C_{SPM}, band ratios of $R_{rs}(671)$, $R_{rs}(745)$, and $R_{rs}(862)$ over $R_{rs}(551)$ are all included to retrieve C_{SPM} for waters from ocean to turbid river mouths. More importantly, we introduce weighting factors

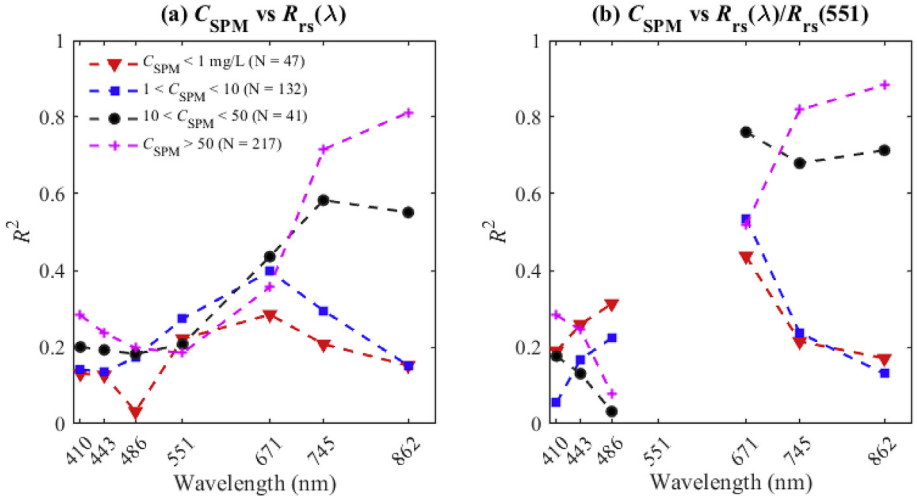

Fig. 3. The determination coefficient (R^2) between C_{SPM} and R_{rs} measurements for separate C_{SPM} ranges. (a) R^2 between C_{SPM} and $R_{rs}(\lambda)$ at a single VIIRS band. (b) R^2 between C_{SPM} and the band ratios of $R_{rs}(\lambda)$ over $R_{rs}(551)$.

to progressively adjust the weights of the three band ratios to effectively account for the shift of the $R_{rs}(\lambda)$ to the C_{SPM}-sensitive wavelength. As a result, a generalized index for SPM (GI_{SPM}) is formulated,

$$GI_{SPM} = c_0 \times \frac{R_{rs}(551)}{R_{rs}(486)} + \sum_{i=1}^{3} c_i \times W_i \times \frac{R_{rs}(\lambda_i)}{R_{rs}(551)} \quad (5)$$

where $c_{0\text{-}3}$ are empirical coefficients, and $W_{1\text{-}3}$ are the weighting factors for $R_{rs}(\lambda)$ at λ_1 (671 nm), λ_2 (745 nm), and λ_3 (862 nm), respectively. W_i is defined as,

$$W_i = \frac{R_{rs}(\lambda_i)}{R_{rs}(\lambda_1) + R_{rs}(\lambda_2) + R_{rs}(\lambda_3)}, \quad i = 1, \ 2, \ 3 \quad (6)$$

The band ratio $R_{rs}(551)/R_{rs}(486)$ in Eq. (5) is introduced to partially and empirically account for the variation of chlorophyll-a concentration in clear and low turbidity waters, as it may also contribute to the ratio of $R_{rs}(671)/R_{rs}(551)$. The SPM concentration is finally calculated from the GI_{SPM} using a power-law function,

$$C_{SPM} = a_1 \times [GI_{SPM}]^{a_2} \quad (7)$$

where a_1 and a_2 are the algorithm coefficients. Values of the algorithm constants ($c_{0\text{-}3}$ and $a_{1\text{-}2}$) in Eq. (5) and Eq. (7) were calculated from nonlinear least-square-fit using paired C_{SPM} and $R_{rs}(\lambda)$ ratios from the *in situ* datasets, with results as 20.43, 2.15, 0.04, 1.17, 0.4, and 14.86 for a_1, a_2, c_0, c_1, c_2, and c_3, respectively (also see Table 2). Note that it is dimensionless for the coefficients $c_{0\text{-}3}$ and a_2, while the units for a_1 is mg/L.

2.3.2. Other retrieval algorithms for C_{SPM}

Table 3 lists a few typical algorithms in the literature that are employed in this study for algorithm inter-comparison. The second column in Table 3 presents the algorithm formulae and coefficients as in the literature, while the third column shows adjusted algorithm coefficients that are recalibrated using the *in situ* datasets of this effort. The Dsa_07 (D'Sa et al., 2007) was explicitly proposed for relatively clear waters and was recalibrated using data with C_{SPM} < 50 mg/L only. The Doxaran_02 (Doxaran et al., 2002a) and He_13 (He et al., 2013) were perceived appropriate for turbid waters only, and they were therefore recalibrated using data with C_{SPM} > 50 mg/L. The Geostationary Ocean Color Imager (GOCI) algorithm in Table 3 is the standard C_{SPM} algorithm for processing GOCI data, which employs two respective algorithms for less-turbid and turbid waters (Min et al., 2013; Siswanto et al., 2011). In this study, GOCI and Shen_10 (Shen et al., 2010b) used the same hard-wired switching scheme to estimate C_{SPM} for less turbid waters (C_{SPM} < 50 mg/L) and highly turbid waters (C_{SPM} > 50 mg/L), with a switching threshold of $R_{rs}(671)$ = 0.02 sr^{-1}. We followed this approach for consistency, also because 97% of highly turbid samples in our datasets having $R_{rs}(671)$ > 0.02 sr^{-1} and 94% of the less-turbid samples having $R_{rs}(671)$ < 0.02 sr^{-1}.

In addition to the relatively simple empirical algorithms described in Table 3, we also included Mao_12 (Mao et al., 2012), Dogliotti_15 (Dogliotti et al., 2015), Han_16 (Han et al., 2016), Novoa_17 (Novoa et al., 2017), and Gohin_05 (Gohin et al., 2005) for algorithm inter-comparison. The first four algorithms were proposed to retrieve wide-range C_{SPM} with a smooth transition from relatively clear to highly turbid waters, while Gohin_05 was for relatively clear waters only.

2.3.2.1. The Mao_12 algorithm. The Mao_12 algorithm uses a rather complicated system with four indices to formulate a proxy (P) for C_{SPM}. Steps to illustrate the Mao_12 algorithm are summarized below,

$$X1 = (R_{rs}(\lambda))/(\eta - R_{rs}(\lambda)) \quad (8)$$

$$X2 = (R_{rs}(\lambda_1))/(R_{rs}(\lambda_2)) \quad (9)$$

$$X3 = \sum R_{rs}(\lambda_i) \quad (10)$$

$$X4 = \sum \delta R_{rs}(\lambda_i)/\delta\lambda_i \quad (11)$$

$$P = (f_1X1 + f_2X2 + f_3X3 + f_4X4)/\sum_{i=1}^{4} f_i \quad (12)$$

$$C_{SPM} = 10^{(b_1+b_2*P)} \quad (13)$$

where $X1$, $X2$, $X3$, and $X4$ are the four indices, and the wavelengths in each index are selected based on the highest correlation coefficients of the regression analysis between the index and C_{SPM}. η in Eq. (8) is determined along with the selected wavelength for $X1$. $X4$ is the sum of the spectral slope at each wavelength, which is calculated from the derivation of two neighboring $R_{rs}(\lambda)$ in relation to their wavelengths.

The Mao_12 algorithm was initially calibrated at the center bands of Sea-viewing Wide Field-of-view Sensor (SeaWiFS), which are 412, 443, 490, 510, 555, 670, 765, and 865 nm, respectively. Specifically, $X1$ is computed at 670 nm with η as 0.085. $X2$ is the band ratio of R_{rs}(765) to

Table 2
Empirical coefficients of the proposed GAA_{SPM} calibrated by the four *in situ* datasets.

Coefficients	a_1 (mg/L)	a_2	c_0	c_1	c_2	c_3
Values	20.43	2.15	0.04	1.17	0.4	14.86

Table 3
Quantitative C_{SPM} retrieval algorithms from peer-reviewed articles.

Algorithm	Original	Recalibrated	Remarks
Dsa_07	C_{SPM} = 10^(1.25 + 1.11 × log10(X))	C_{SPM} = 10^(-0.44 + 1.93 × log10(X))	X = $R_{rs}(671)/R_{rs}(551)$
He_13	C_{SPM} = 10^(1.076 + 1.123 X)	C_{SPM} = 10^(1.14 + 0.92 X)	X = $R_{rs}(745)/R_{rs}(486)$
Doxaran_02	C_{SPM} = exp(3.132 X+3.01)	C_{SPM} = exp(2.8 X+3.53)	X = $R_{rs}(862)/R_{rs}(551)$
GOCI	C_{SPM} = 10^(0.088 + 1.627 X1 +1.121 X2)	C_{SPM} = 10^(1.92 + 1.35 X1 -0.26 X2)	$C_{SPM} \geq 50$ mg/L X1 = $R_{rs}(745)/R_{rs}(551)$ X2 = $R_{rs}(671)/R_{rs}(486)$
	C_{SPM} = 10^(0.649 + 25.623 X1 -0.646 X2)	C_{SPM} = 10^(0.59 + 13.5 X1 -0.66 X2)	$C_{SPM} < 50$ mg/L X1 = $R_{rs}(551) + R_{rs}(671)$ X2 = $R_{rs}(486)/R_{rs}(551)$
Shen_10	C_{SPM} = 2 × 0.078 X/(10.629 × (0.078-X)^2)	C_{SPM} = 2 × 7.75 X/(0.0004 × (7.75-X)^2)	$C_{SPM} < 50$ mg/L X = $R_{rs}(671)$
	C_{SPM} = 2 × 0.104 X/(1.804 × (0.104-X)^2)	C_{SPM} = 2 × 0.11 X/(0.002 × (0.11-X)^2)	$C_{SPM} \geq 50$ mg/L X = $R_{rs}(862)$

$R_{rs}(510)$. $X3$ is the sum of $R_{rs}(\lambda)$ at 510 and 765 nm. $X4$ is the sum of spectral slopes at all SeaWiFS bands except 412 and 865 nm. The original values of $f_{1\text{-}4}$ and $b_{1\text{-}2}$ are 0.3, 0.2, 10, 1, 0.947, and 0.775, respectively. These empirical coefficients are re-tuned using our datasets with wavelengths for each index selected from the VIIRS center bands. As a result, $X1$ is computed from $R_{rs}(862)$ with η now as 0.075. $X2$ is the band ratio of $R_{rs}(862)$ to $R_{rs}(551)$. $X3$ is the sum of $R_{rs}(\lambda)$ at 671, 745, and 862 nm. $X4$ is the sum of spectral slopes at all VIIRS-SNPP bands except for 410 and 862 nm. The recalibrated values of $f_{1\text{-}4}$ and $b_{1\text{-}2}$ are −0.49, 1.22, 9.37, 0.37, 14.29, and −0.08, respectively.

2.3.2.2. The Dogliotti_15 algorithm. Nechad et al. (2010) proposed a generic algorithm to directly retrieve C_{SPM} from a single band water-leaving reflectance ($\rho_w(\lambda) = \pi R_{rs}(\lambda)$, dimensionless). Dogliotti et al. (2015) adapted the Nechad et al. (2010) algorithm and used two respective algorithms to retrieve C_{SPM} for relatively clear and turbid waters,

$$C_{SPM\_clear} = A_T(\lambda_1)\rho_w(\lambda_1)/(1 - \rho_w(\lambda_1)/C(\lambda_1)) \quad (14)$$

$$C_{SPM\_tur} = A_T(\lambda_2)\rho_w(\lambda_2)/(1 - \rho_w(\lambda_2)/C(\lambda_2)) \quad (15)$$

where $A_T(\lambda)$ and $C(\lambda)$ are wavelength-dependent calibration coefficients and λ_1 and λ_2 are set to 645 and 859 nm, respectively. The originally values of $A_T(\lambda)$ and $C(\lambda)$ were 228.1 and 0.164 for λ_1, and 3078.9 and 0.211 for λ_2, respectively. A switching scheme was also proposed where $C_{SPM} = C_{SPM\_clear}$ when $\rho_w(645) < 0.05$ and $C_{SPM} = C_{SPM\_tur}$ when $\rho_w(645) > 0.07$. For $\rho_w(645)$ between 0.05 and 0.07, $C_{SPM} = (1\text{-}w)\ C_{SPM\_clear} + w\ C_{SPM\_tur}$, with w as the weighting factor changed linearly from 0 at $\rho_w(645) = 0.05$ to 1 at $\rho_w(645) = 0.07$.

In this study, we recalibrated the Dogliotti_15 algorithm for VIIRS bands (*i.e.* λ_1 = 671 nm and λ_2 = 862 nm) using the four *in situ* datasets, with recalibrated $A_T(\lambda)$ and $C(\lambda)$ as 227.5 and 0.1736 for λ_1, and 2485.1 and 0.2155 for λ_2, respectively. The same switching and blending schemes were adopted here but using $\rho_w(671)$ values as the switching boundaries.

2.3.2.3. The Han_16 algorithm. Han et al. (2016) also developed two algorithms for clear and turbid waters based on the algorithm of Nechad et al. (2010). The same Eqs. (14) and (15) are employed for Han_16, but with λ_1 and λ_2 set to 671 and 745 nm, respectively. Note that Han_16 also provides an option of using $\rho_w(671)$ to estimate C_{SPM} for turbid waters, which is not considered in this study due to the saturation of $\rho_w(671)$ over extremely turbid waters (Shi and Wang, 2014). The original $A_T(\lambda)$ and $C(\lambda)$ in Han et al. (2016) were set to 389.5 and 0.5 for 671 nm, and 2220.1 and 0.4 for 745 nm, respectively. In this study, $A_T(\lambda)$ and $C(\lambda)$ were recalibrated using our datasets, and the optimized values are 227.2 and 0.35 for 671 nm, and 2338.8 and 0.23 for 745 nm, respectively. Han et al. (2016) proposed a different blending scheme from Dogliotti_15, which is expressed as,

$$C_{SPM} = \frac{W_c * C_{SPM\_clear} + W_t * C_{SPM\_tur}}{W_c + W_t} \quad (16)$$

where W_c and W_t are the weights for the estimated C_{SPM} for clear and turbid waters, respectively, and are calculated from $R_{rs}(671)$. Specifically, for $R_{rs}(671) < 0.03\ sr^{-1}$, W_c is set to 1 and W_t is set to 0. For $R_{rs}(671) > 0.04\ sr^{-1}$, W_c is set to 0 and W_t is set to 1. For $R_{rs}(671)$ between the two boundaries, W_c and W_t are defined as,

$$W_c = log10(0.04) - log10[R_{rs}(671)] \quad (17)$$

$$W_t = log10[R_{rs}(671)] - log10(0.03) \quad (18)$$

2.3.2.4. The Novoa_17 algorithm. Novoa et al. (2017) proposed a multi-conditional algorithm for C_{SPM} retrieval, which switches among five different algorithms based on the $\rho_w(671)$ values. The Novoa_17 algorithm is described in Table 4. The 'Original' expressions in Table 4 employ the calibrated coefficients from Novoa et al. (2017), while the 'Recalibrated' expressions use coefficients recalibrated from the *in situ* datasets of this study. Novoa_17 has three key algorithms (C_{SPM_Green}, C_{SPM_Red}, and C_{SPM_Green} in Table 4) for clear, moderately turbid, and highly turbid waters, respectively, and uses two blending algorithms ($C_{SPM\_Green\text{-}Red}$ and $C_{SPM\_Red\text{-}NIR}$) to obtain smooth transitions of the estimated C_{SPM}. The weighting factors ($\alpha_{1\text{-}2}$ and $\beta_{1\text{-}2}$) for $C_{SPM\_Green\text{-}Red}$ and $C_{SPM\_Red\text{-}NIR}$ in Table 4 are calculated as following,

$$\alpha_1 = \ln\left(\frac{S_{L95+}}{\rho_w(671)}\right)/\ln\left(\frac{S_{L95+}}{S_{L95-}}\right), \beta_1 = \ln\left(\frac{\rho_w(671)}{S_{L95-}}\right)/\ln\left(\frac{S_{L95+}}{S_{L95-}}\right) \quad (19)$$

$$\alpha_2 = \ln\left(\frac{S_{H95+}}{\rho_w(671)}\right)/\ln\left(\frac{S_{H95+}}{S_{H95-}}\right), \beta_2 = \ln\left(\frac{\rho_w(671)}{S_{H95-}}\right)/\ln\left(\frac{S_{H95+}}{S_{H95-}}\right) \quad (20)$$

where S_{L95+} and S_{L95-} are the lower smoothing bounds derived from the 95% confidence levels of the regression curve between $\rho_w(671)$ and $\rho_w(551)$, while S_{H95+} and S_{H95-} are the higher smoothing bounds derived from the $\rho_w(862)$-$\rho_w(671)$ regression curve (See Fig. 4 in Novoa et al. (2017) for details). S_{L95+}, S_{L95-}, S_{H95+}, and S_{H95-} are provided in Novoa et al. (2017) with values of 0.007, 0.016, 0.08, and 0.2, respectively, for Gironde estuary measurements. We adopted these values to evaluate the validity of Novoa_17 in this study.

2.3.2.5. Gohin_05 algorithm. Gohin et al. (2005) assumed that C_{SPM} could be estimated as the sum of the concentrations by non-living SPM (SPM_{nLv}) and organic SPM (SPM_o). Specifically, SPM_{nLv} can be derived

Table 4
The multi-conditional Novoa_17 algorithm for C_{SPM} retrieval. The weighting factors ($\alpha_{1\text{-}2}$ and $\beta_{1\text{-}2}$) for $C_{SPM\_Green\text{-}Red}$ and $C_{SPM\_Red\text{-}NIR}$ are calculated following Eqs. (19) - (20) in the text.

ρ_w (671) values	SPM algorithm	Expressions	
		Original	Recalibrated
< 0.007	C_{SPM_Green}	96.6 ρ_w (551)	93.5 ρ_w (551)
(0.007; 0.016)	$C_{SPM\_Green\text{-}Red}$	$\alpha_1\ C_{SPM\_Green} + \beta_1\ C_{SPM\_Red}$	
(0.016; 0.08)	C_{SPM_Red}	575.8 ρ_w (671)	529.3 ρ_w (671)
(0.08; 0.12)	$C_{SPM\_Red\text{-}NIR}$	$\alpha_2\ C_{SPM\_Red} + \beta_2\ C_{SPM\_NIR}$	
> 0.12	C_{SPM_NIR}	32110 $\rho_w(862)^2$ + 2204 $\rho_w(862)$	73489 $\rho_w(862)^2$ - 1389.5 $\rho_w(862)$

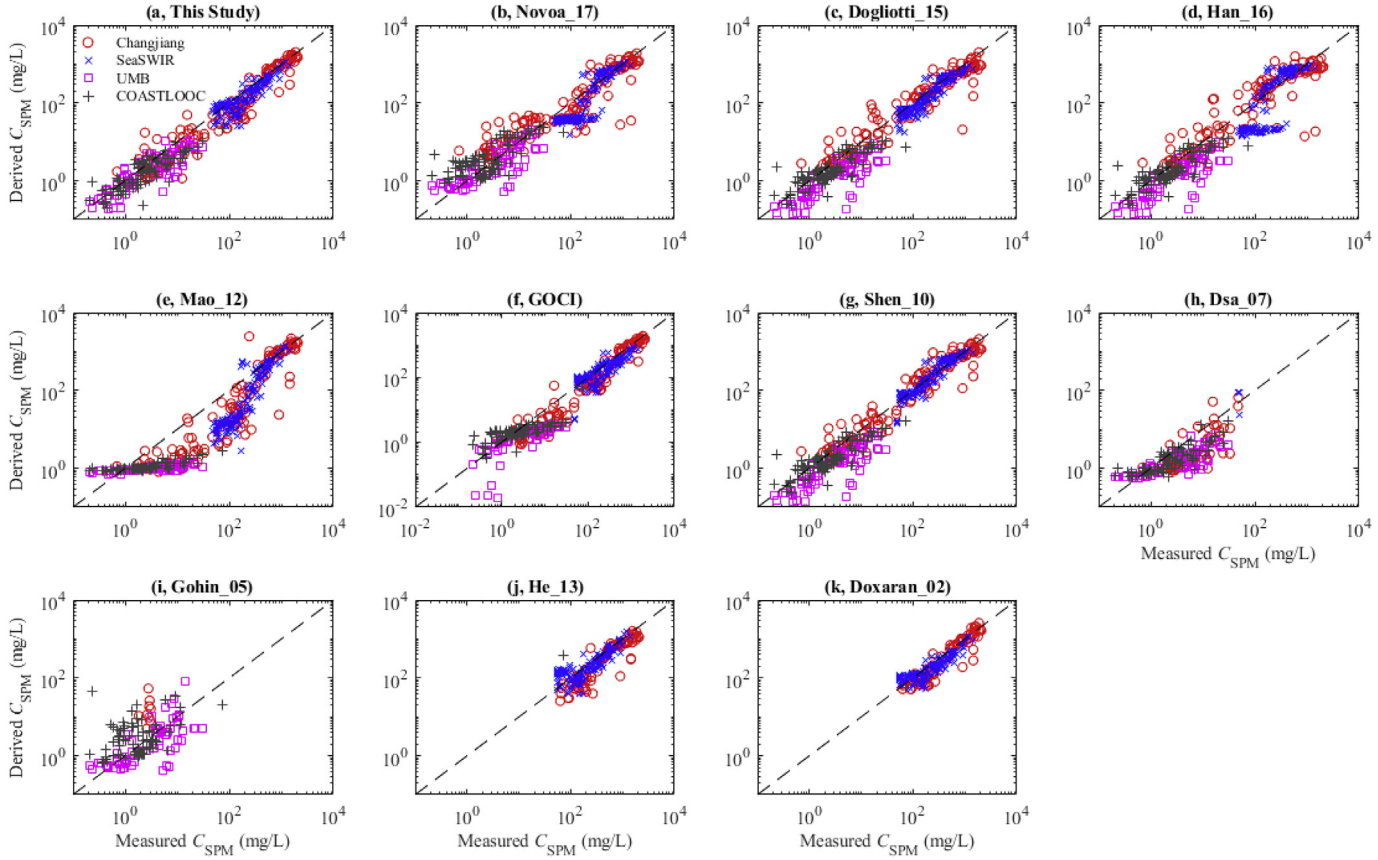

Fig. 4. Validation and inter-comparison of C_{SPM} retrieval algorithms. Panels (h) and (i) present the validation results of Dsa_07 and Gohin_05 for $C_{SPM} < 50$ mg/L, while panels (j) and (k) show the validation results of He_13 and Doxaran_02 for $C_{SPM} > 50$ mg/L.

from normalized water-leaving reflectance at the green or red bands with assumptions of constant mass-specific particulate absorption and backscattering coefficients (See their Eq. (18) and Table 3 for details). The SPM_o can be converted from the concentration of particulate organic carbon (POC), which can be estimated from chlorophyll-a concentration ([Chl]). As a result, the Gohin_05 algorithm can be expressed as,

$$C_{SPM} = SPM_{nLv} + 234[Chl]^{0.57}, \quad (21)$$

where [Chl] is retrieved from a five-band algorithm using a specific look-up-table (LUT) (Gohin et al., 2002). Note that the recalibration of Gohin_05 was not performed in this study, given that only a few [Chl] measurements in our datasets can be found to update the LUT. Therefore, in this study, we evaluate the performance of Gohin_05 using its original LUT and mass-specific particulate absorption and backscattering coefficients, provided by Dr. Francis Gohin at the authors' request.

2.4. Statistical measures for model performance

To evaluate the performance of each algorithm, several statistical measures were introduced in this study, including the slope, the coefficient of determination (R^2), the relative mean absolute difference (rMAD), and the root mean square difference (RMSD). The slope and R^2 are computed from the linear regression between the measured and the derived C_{SPM} using the Model-II regression (Laws, 1997). The rMAD and RMSD are defined by,

$$rMAD = \sum |1 - derived/measured| / N \times 100\% \quad (22)$$

$$RMSD = \sqrt{\sum (derived - measured)^2 / N} \quad (23)$$

where N is the number of data points.

The performances of the abovementioned algorithms from the literature were first evaluated by applying them to the four *in situ* datasets using their original algorithm coefficients. Statistic measures are tabulated in Table 5, where the derived C_{SPM} from these algorithms are found with relatively large uncertainties, except for the Doxaran_02. Such performances are likely due to both data characteristics and data processing, as empirical algorithms are always data dependent. Therefore, a re-tuning of the algorithm coefficients is necessary to ensure apple-to-apple comparisons between these algorithms and GAA_{SPM}.

For the recalibrated algorithms, model win rate (MWR) (Seegers et al., 2018) is adopted here as an additional metric to evaluate the algorithm performance. A pair-wise comparison of the absolute residual difference (= |derived – measured|) was performed for each sample, and the algorithm with a lower residual was designated as the winner. MWR is defined as the percent wins for each algorithm. In this study, each algorithm was pair-to-pair compared to other candidate algorithms to calculate the MWR. We adopted the average MWR of each algorithm as the metric to evaluate its overall performance, which is hereafter referred to as the overall win rate (OWR).

3. Results

3.1. Inter-comparison of C_{SPM} retrieval algorithms

Validation results of GAA_{SPM}, as well as these recalibrated algorithms described in Section 2.3, are presented in Fig. 4. Considering the applicable range of each C_{SPM} algorithm, the performance of each algorithm was evaluated for the entire C_{SPM} range, the subset of less turbid waters ($C_{SPM} < 50$ mg/L), and the subset of highly turbid waters

Table 5
Statistics of the quantitative C_{SPM} retrieval algorithms using their original empirical coefficients.

		Novoa_17	Dogliotti_15	Han_16	Mao_12	GOCI	Shen_10	Dsa_07	Gohin_05	He_13	Doxaran_02
All (N = 437)	Slope	0.73	1.17	0.46	0.00	34.34	1.08	NA	NA	NA	NA
	R^2	0.78	0.80	0.65	0.52	0.79	0.78	NA	NA	NA	NA
	rMAD (%)	78.6	55.1	62.7	290.5	1159.7	168.5	NA	NA	NA	NA
	RMSD	191.8	204.6	273.4	427.5	13771.7	196.8	NA	NA	NA	NA
SPM < 50 mg/L (N = 214)	Slope	1.58	2.10	1.76	0.04	12.76	12.48	5.85	2.32	NA	NA
	R^2	0.53	0.44	0.40	0.50	0.03	0.13	0.66	0.07	NA	NA
	rMAD (%)	114.3	64.5	77.9	479.5	140.8	290.3	1921.9	277.63	NA	NA
	RMSD	10.5	14.9	12.7	9.3	116.5	114.0	67.2	9.91	NA	NA
SPM > 50 mg/L (N = 223)	Slope	0.70	1.16	0.41	0.00	36.93	1.04	NA	NA	1.83	0.96
	R^2	0.69	0.72	0.50	0.35	0.74	0.74	NA	NA	0.80	0.83
	rMAD (%)	41.3	45.3	46.9	93.6	2221.5	41.6	NA	NA	79.8	36.9
	RMSD	273.8	292.0	390.5	610.9	19679.5	256.1	NA	NA	534.3	218.0

* NA indicates no information available or not applicable.

Table 6
Statistics of the derived C_{SPM} by quantitative C_{SPM} retrieval algorithms with recalibrated empirical coefficients using the four *in situ* datasets of this study.

		This Study	Novoa_17	Dogliotti_15	Han_16	Mao_12	GOCI	Shen_10	Dsa_07	He_13	Doxaran_02
All (N = 437)	Slope	0.91	0.92	0.74	0.84	1.00	0.87	0.91	NA	NA	NA
	R^2	0.91	0.80	0.80	0.67	0.79	0.90	0.82	NA	NA	NA
	rMAD (%)	41.3	76.2	44.6	61.2	64.6	46.3	42.5	NA	NA	NA
	RMSD	122.0	171.8	183.8	219.6	183.4	128.6	162.8	NA	NA	NA
	OWR (%)	57.9	48.9	58.0	46.7	29.0	52.7	56.8	NA	NA	NA
SPM < 50 mg/L (N = 214)	Slope	0.97	1.11	1.38	1.87	0.26	0.46	0.60	1.13	NA	NA
	R^2	0.59	0.55	0.46	0.27	0.36	0.17	0.51	0.52	NA	NA
	rMAD (%)	50.0	102.9	56.3	60.0	67.5	59.6	52.1	53.3	NA	NA
	RMSD	6.5	7.2	9.4	14.7	9.5	9.3	7.1	7.9	NA	NA
	OWR (%)	57.3	48.3	52.7	57.6	27.7	50.2	46.7	46.4	NA	NA
SPM > 50 mg/L (N = 223)	Slope	0.94	0.93	0.72	0.80	1.07	0.89	0.87	NA	0.77	1.00
	R^2	0.88	0.72	0.72	0.53	0.74	0.87	0.74	NA	0.80	0.85
	rMAD (%)	32.2	48.3	32.4	62.4	61.7	32.4	32.6	NA	42.5	31.6
	RMSD	174.2	245.4	262.5	313.5	262.0	183.6	232.5	NA	224.2	188.4
	OWR (%)	54.4	45.7	59.6	31.6	30.0	51.9	64.7	NA	52.7	59.3

* NA indicates no information available or not applicable.

(C_{SPM} > 50 mg/L), respectively. Statistic measures of each algorithm for the three C_{SPM} range are given in Table 6.

Evaluation of algorithms over the entire C_{SPM} range shows that GAA_{SPM} has the best performance with points more closely distributed to the 1:1 line (Fig. 4a). GAA_{SPM} also has the highest R^2 (0.91), and the smallest rMAD (41.3%) and RMSD (122.0 mg/L) for the derived C_{SPM} among all algorithms that have valid retrievals over the entire C_{SPM} range (Table 6). Dogliotti_15 and Shen_10 also have comparable C_{SPM} retrieval accuracy with GAA_{SPM} with rMADs of 44.6% and 42.5%, respectively, followed by the GOCI with an rMAD of 46.3%. The OWRs of GAA_{SPM}, Dogliotti_15, and Shen_10 over the entire C_{SPM} range also confirm their comparable performance, with the values of 57.9%, 58.0, and 56.8%, respectively. Note that the performance of GAA_{SPM}, Dogliotti_15, GOCI, and Shen_10 in highly turbid waters are very consistent (rMAD ~ 32%). Therefore, the better performance of GAA_{SPM} over the entire C_{SPM} range is because GAA_{SPM} also performs well in less turbid waters (Table 6).

In addition, including OWR as one of the metrics allows for a better understanding of the error distribution for each algorithm. For example, the performance of Shen_10 and GAA_{SPM} in highly turbid waters are very comparable in terms of rMAD (32.6% and 32.2%, respectively), but OWR of Shen_10 (= 64.7%) is much higher than that of GAA_{SPM} (= 54.4%), suggesting that more retrievals from Shen_10 are with large residuals, or 'outliers'. Detailed discussion on these different metrics and their advantages and disadvantages can be referred to Seegers et al. (2018).

Other algorithms capable of wide-range C_{SPM} retrieval, Novoa_17, Han_16, and Mao_12, are found with relatively larger uncertainties in terms of both rMAD and RMSD. Mao_12 is observed with significant uncertainties for highly turbid waters with an rMAD of 61.7%, which is mainly attributed to the significantly underestimated C_{SPM} within the 50–400 mg/L range (see Fig. 4e). The relatively larger uncertainties of Novoa_17 and Han_16 are also attributed to the retrievals in moderately turbid waters, especially for those of the SeaSWIR dataset (see Figs. 4b and d). In addition, Han_16 uses R_{rs}(745) instead of R_{rs}(862) for C_{SPM} retrieval in extremely turbid waters, which results in saturated retrievals of C_{SPM}.

Dsa_07 and Gohin_05 were explicitly developed for less turbid waters. However, evaluations of Dsa_07 and Gohin_05 show that they have relatively larger uncertainties compared with GAA_{SPM}. For Dsa_07, it appears that the algorithm is no longer sensitive for C_{SPM} below 5 mg/L (Fig. 4h). For Gohin_05, as it has not been recalibrated or optimized using our datasets, the relatively larger uncertainties could be expected (Fig. 4i).

Evaluation results of Doxaran_02 and He_13, explicitly proposed for highly turbid waters, are presented in Figs. 4j and k, respectively. Doxaran_02 has been observed with the smallest rMAD of 31.6%, followed by GAA_{SPM} with an rMAD of 32.2%. He_13, on the other hand, has relatively larger uncertainties with an rMAD of 42.5%, which is likely because that He_13 utilizes R_{rs}(745) instead of R_{rs}(862) for C_{SPM} retrieval, as R_{rs}(862) is more sensitive to C_{SPM} of highly turbid waters. However, it appears that GAA_{SPM} could arguably perform the best for the turbid subset as GAA_{SPM}-retrieved C_{SPM} has the highest R^2 (0.88) and smallest RMSD (174.23 mg/L) among all algorithms (Table 6).

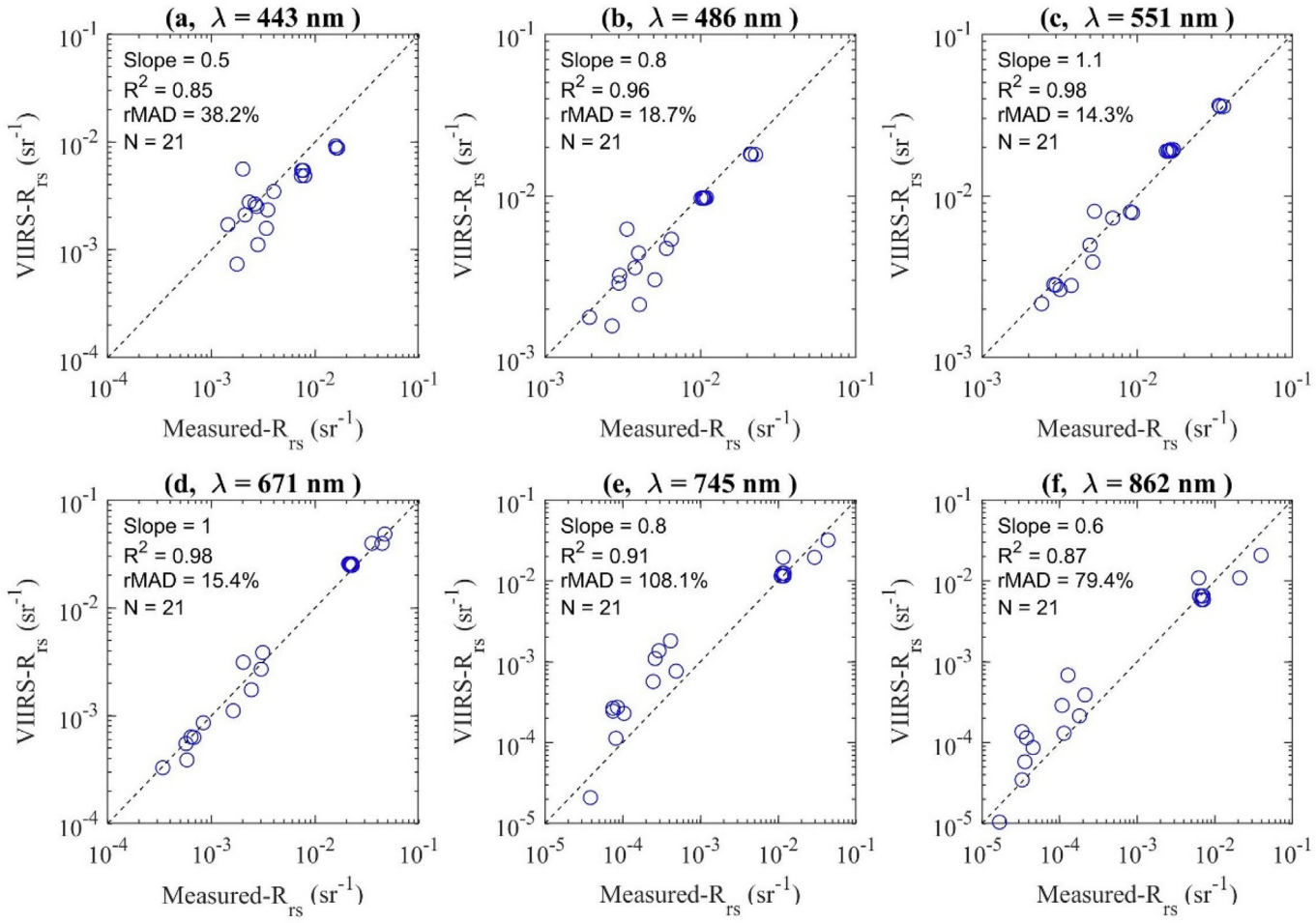

Fig. 5. Validation of VIIRS NIR-SWIR $R_{rs}(\lambda)$ product against field measurements collected within 1 h of the acquisition of the VIIRS image.

Further discussions of GAA_{SPM} are presented in Section 4.1.

3.2. SPM mapping products

The NIR-SWIR atmospheric correction algorithm was first evaluated by comparing satellite-derived $R_{rs}(\lambda)$ with match-up $R_{rs}(\lambda)$ from ground measurements, which is presented in Fig. 5. Overall, good agreements are observed between the field-measured $R_{rs}(\lambda)$ and the VIIRS-derived $R_{rs}(\lambda)$ at 486, 551, and 671 nm, with rMADs of 18.7%, 14.3%, and 15.4%, respectively. However, significant uncertainties are observed for VIIRS-derived $R_{rs}(\lambda)$ at 443, 745, and 862 nm, with rMADs of 38.2%, 108.1%, and 79.4%, respectively. Since the band 443 nm is not involved in GAA_{SPM}, the uncertainties of VIIRS $R_{rs}(443)$ will not be discussed in this study. The large uncertainties of $R_{rs}(745)$ and $R_{rs}(862)$ are mainly observed in relatively clear waters, but their impacts on the derived C_{SPM} by GAA_{SPM} can be neglected in such waters (see discussions in Section 4.2). Note that validation of the NIR-SWIR atmospheric correction algorithm was not performed for extremely turbid waters due to no available match-ups in this study. However, previous efforts have demonstrated that the NIR-SWIR algorithm could yield accurate R_{rs}(NIR) over turbid coastal and estuarine waters for multiple satellite data, including the VIIRS-SNPP (Wang et al., 2007, 2011). Therefore, the NIR-SWIR atmospheric correction is deemed to be adequate for C_{SPM} retrieval in both clear and turbid waters.

In this study, as demonstrations, GAA_{SPM} was applied to VIIRS-SNPP $R_{rs}(\lambda)$ products to map the spatial distribution of C_{SPM} over two highly turbid estuaries: China's Changjiang estuary and Argentina's Río de La Plata estuary. The recalibrated Novoa_17, Dogliotti_15, Shen_10, GOCI, and Mao_12 algorithms were also implemented to the same VIIRS-SNPP data for algorithm inter-comparison.

The six C_{SPM} retrieval algorithms were first implemented to a VIIRS-SNPP image acquired on April 8, 2018, over the Changjiang estuary with the C_{SPM} mapping products presented in Figs. 6a–f. Overall, the C_{SPM} mapping products by the six algorithms present similar patterns in the spatial distribution where high C_{SPM} is frequently found in the Subei Coast and the Hangzhou Bay (see their respective locations in Fig. 6a). A decreasing trend of C_{SPM} can be observed from the coast to the offshore waters, and rapid declines of C_{SPM} occur at the front of the turbidity plume. The major differences among these mapping products lie in the range of the derived C_{SPM}, especially for C_{SPM} in the offshore areas and the turbidity maxima zone.

It is difficult to quantitatively evaluate the accuracy of the C_{SPM} maps due to the lack of high-quality satellite-ground match-ups. Notably, the spatial variation of the "ground-truth" C_{SPM} at the VIIRS pixel scale (750 m × 750 m) cannot be neglected for turbid estuaries. As a result, discrepancies between VIIRS-derived and *in situ*-measured C_{SPM} could be expected even for a "perfect" match-up on time and location, not to mention that VIIRS $R_{rs}(\lambda)$ is derived from a 3-by-3-pixel window. However, the ranges of the derived C_{SPM} by the six algorithms could give some insights into their respective performances. For the offshore waters, the derived C_{SPM} by GAA_{SPM}, Dogliotti_15, Mao_12, and GOCI are overall comparable, while Shen_10 produces much lower $C_{SPM,}$ and Novoa_17 yields relatively higher C_{SPM}. As an indirect validation, the measured C_{SPM} at the offshore area, highlighted in Fig. 6b with the red dashed rectangle, in March of 2013 was between 0.7 and 6.8 mg/L with an average C_{SPM} of 3.4 mg/L (N = 14), which agrees well

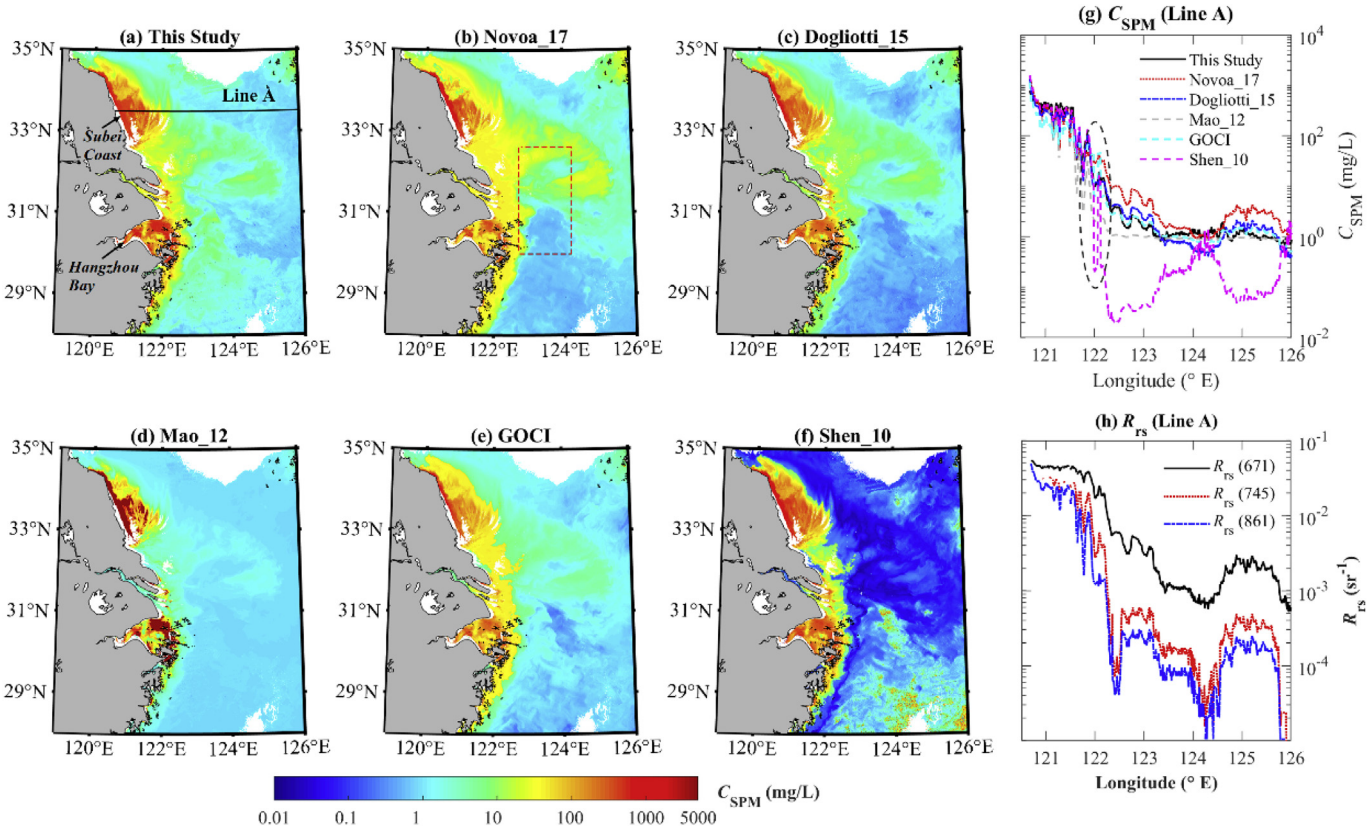

Fig. 6. VIIRS-SNPP C_{SPM} mapping products over the Changjiang estuarine and coastal waters derived by GAA_{SPM} (a), Novoa_17 (b), Dogliotti_15 (c), Mao_12 (d), GOCI (e), and Shen_10 (f), respectively. Variations of the derived C_{SPM} from the six algorithms and the VIIRS $R_{rs}(\lambda)$ at 671, 745, and 861 nm along a transect (Lines A in panel (a)) are presented in panels (g) and (h), respectively. Derived C_{SPM} over 5000 mg/L by Mao_12 is not shown in panel (g). The VIIRS-SNPP data is merged from two images acquired at 04:44:20 UTC and 04:45:46 UTC on April 8, 2018.

with the retrievals by GAA_{SPM}, Dogliotti_15, and GOCI (Figs. 6a, c, and e).

Variations of the retrieved C_{SPM} along a transect (Lines A Fig. 6a) also confirm the consistent estimations of C_{SPM} by GAA_{SPM}, Dogliotti_15, and GOCI in offshore waters (see Figs. 6h and i). Compared with GAA_{SPM}, Mao_12 seems to underestimate the C_{SPM} for low and moderate turbidity waters (see Fig. 6h), which is also observed in Fig. 4e. For the turbidity maxima zones in the Hangzhou Bay and the Subei Coast, the derived C_{SPM} ranges by the GAA_{SPM} and Shen_10 are overall comparable, while GOCI predicts slightly lower C_{SPM} and Mao_12 yields much higher C_{SPM}. Compared with GAA_{SPM}, Novoa_17 seems to overestimate C_{SPM} in moderate turbidity waters, such as in the Southern part of the Subei Coast. Dogliotti_15, on the other hand, could probably underestimate C_{SPM} in the turbidity maxima zone in the Hangzhou Bay. As mentioned in Dogliotti et al. (2015), the Dogliotti_15 algorithm tends to saturate in high turbidity waters, which could result in the underestimations of C_{SPM}. As shown in Fig. 4c, we do observe the tendency of underestimation of Dogliotti_15-derived C_{SPM} for $C_{SPM} > 1000$ mg/L. Note that measured C_{SPM} from the turbid zones in the Hangzhou Bay reached 2000 mg/L in February, which is close to the predicted results by GAA_{SPM} and Shen_10. Therefore, we could argue that VIIRS-derived C_{SPM} by the GAA_{SPM} and Shen_10 in turbid waters could be more reasonable. However, further evaluation with rigorously matched ground measurements is still required, since C_{SPM} in the Changjiang estuary frequently changes in both magnitude and the spatial distribution.

In addition, discontinuities of the derived C_{SPM} are observed at the front of the turbidity plume by Shen_10 and GOCI, as shown in Figs. 6e and f, which are attributed to the same hard-wired switching scheme employed by these two algorithms. For areas straddling the threshold pixel with $R_{rs}(670) = 0.02\ sr^{-1}$, two different algorithms were applied to derive C_{SPM}, which causes a sudden change of the derived C_{SPM} for the neighboring pixels. The numerical discontinuities of VIIRS-derived C_{SPM} by Shen_10 and GOCI are better visualized by the variations of the derived C_{SPM} along the one transect from the coast to the outer shelf (Line A in Fig. 6a). Transect A spans over both clear and highly turbid waters and, therefore, allows synoptic views of the performance of the six algorithms in different types of waters. As highlighted by the dashed ellipse in Fig. 6g, sudden declines of VIIRS-derived C_{SPM} by Shen_10 and GOCI are observed around the threshold pixel, with the derived C_{SPM} varies by 1–2 orders of magnitude for the two neighboring pixels. Although there might exist real discontinuities of C_{SPM} in natural waters, such discontinuities should also be reflected in R_{rs} measurements. However, $R_{rs}(671)$ along the transect A shows rapid decreases at the front of the turbidity plume but no sudden and significant drop in values (see Fig. 6h). Therefore, the discontinuities observed in the C_{SPM} mapping products of Shen_10 and GOCI are directly introduced by the hard-wired switching schemes. The proposed GAA_{SPM}, on the other hand, uses a progressive index and could avoid the numerical discontinuity. The Novoa_17, Dogliotti_15, and Mao_12 algorithms can provide continuous C_{SPM} maps as well, but their overall performance is less robust as GAA_{SPM}.

The six algorithms were also employed to map C_{SPM} over another turbid estuary, the Río de La Plata estuary of Argentina, and the C_{SPM} mapping products are presented in Fig. 7. Consistent with the results from the Changjiang estuary shown in Fig. 5, GAA_{SPM} has comparable C_{SPM} retrievals with Shen_10 in relatively turbid waters from the river mouth to the front of turbidity plume, while the derived C_{SPM} by Novoa_17, Dogliotti_15, and GOCI are slightly lower in such an area. Mao_12 predicts the highest C_{SPM} in the turbidity maxima regions and

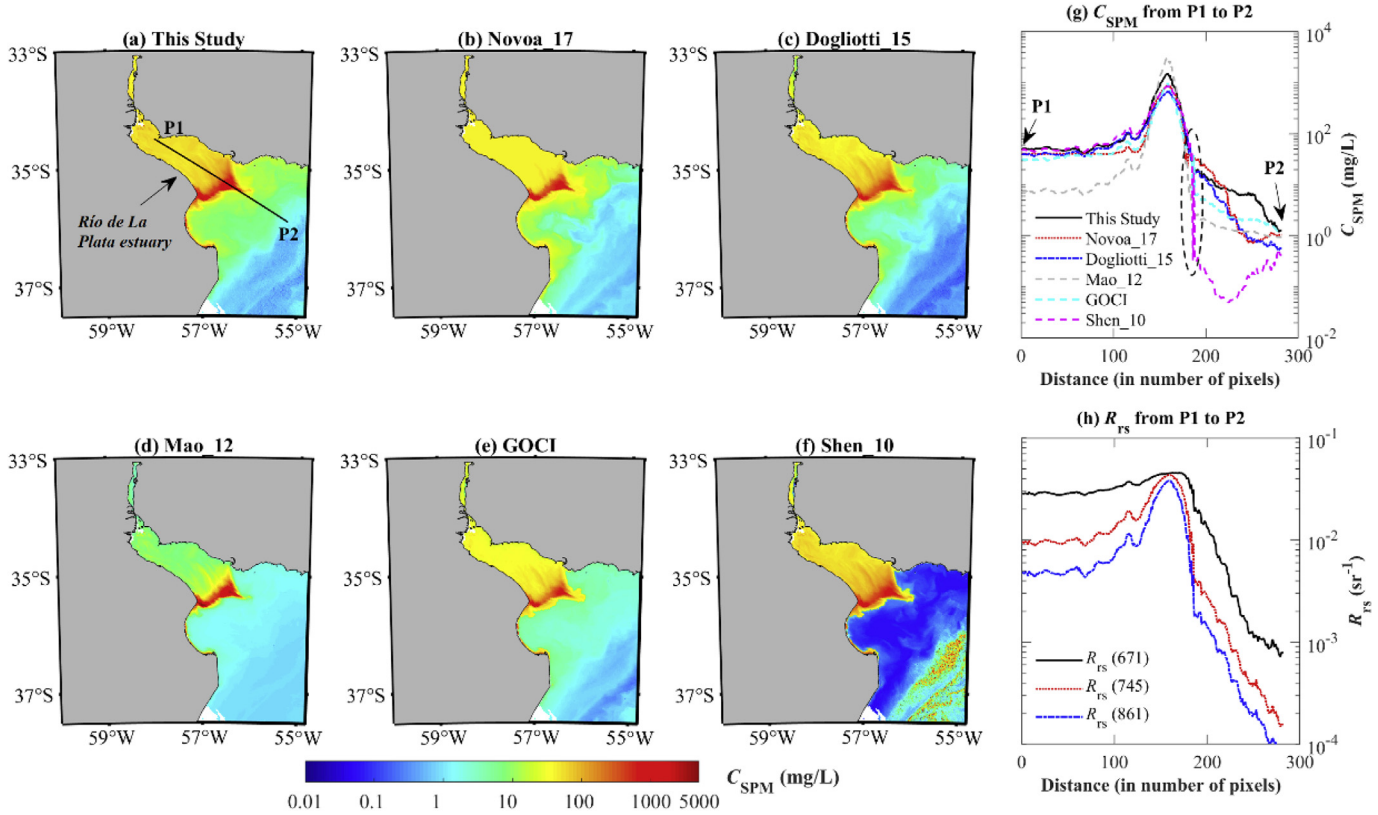

Fig. 7. Same as Fig. 6, but for C_{SPM} mapping products over the Río de La Plata estuary of Argentina. Panels (g) and (h) show the variation of the derived C_{SPM} by the six algorithms and VIIRS $R_{rs}(\lambda)$ at 671, 745, and 861 nm along the transection from P1 to P2 in panel (a). The VIIRS-SNPP data is merged from two images acquired at 18:10:12 UTC and 18:11:37 UTC on November 25, 2017.

becomes insensitive to C_{SPM} variation from the turbidity front to offshore waters (Fig. 7d). Shen_10 systematically underestimates C_{SPM} in less turbid waters with the derived C_{SPM} generally less than 1 mg/L (Fig. 7f). In contrast to Shen_10, the derived C_{SPM} by the GAA_{SPM} in less turbid waters roughly varies between 0.1 and 20 mg/L (Fig. 7a). The performances by the six algorithms in the Río de La Plata estuary have also been evaluated along a transect highlighted in Fig. 7a. All algorithms, except for the Mao_12, have very comparable C_{SPM} retrievals in moderately turbid waters from P1 to the front of the turbidity plume and then have very different performances in the turbidity maxima zone and relatively clear waters. The discontinuity in C_{SPM} spatial distribution is observed from the mapping products of Shen_10 and GOCI (Figs. 7e and f, respectively), which is also highlighted in Fig. 7g.

4. Discussion

4.1. The proposed C_{SPM} retrieval algorithm

The proposed GAA_{SPM} has the overall best performance for the entire C_{SPM} range in this study among all candidate algorithms, which could be attributed to the fact that the GAA_{SPM} takes advantage of the sensitivity of $R_{rs}(\lambda)$ to C_{SPM} in different C_{SPM} ranges. The introduced weighting factors ensure that the generalized index (GI_{SPM}, in Eq. (5)) is dominated by $R_{rs}(671)$ in clear waters and by $R_{rs}(862)$ in highly turbid waters. For instance, as shown in Fig. 8, in relatively clear waters where $C_{SPM} < 10$ mg/L, the weighted $R_{rs}(671)$, defined as $c_1 \times W_1 \times R_{rs}(671)$, according to Eq. (5), is about 1–2 orders of magnitude larger than the weighted $R_{rs}(745)$ and $R_{rs}(862)$, which are defined as $c_2 \times W_2 \times R_{rs}(745)$ and $c_3 \times W_3 \times R_{rs}(862)$, respectively. Therefore, $R_{rs}(671)$ plays a dominant role in GI_{SPM} for such waters. To the contrary, in highly turbid waters, the weighted $R_{rs}(862)$ is about 1–2 orders of magnitude larger than the weighted $R_{rs}(671)$ and $R_{rs}(745)$, and thus

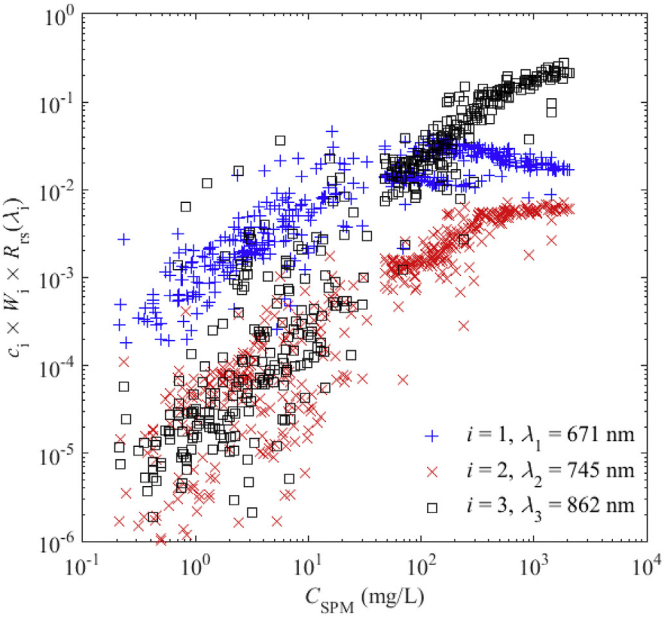

Fig. 8. The contribution of weighted $R_{rs}(\lambda)$ (denoted as $c_i \times W_i \times R_{rs}(\lambda_i)$ in Eq. (5)) at λ_1 (671), λ_2 (745), and λ_3 (862) to the GI_{SPM} with respect to increasing C_{SPM}. The scatter plots are based on the four *in situ* datasets.

dominates the GI_{SPM} in determining C_{SPM}. Therefore, the introduced weighting system can successfully and seamlessly adjust the role of each band to ensure a progressive application of $R_{rs}(\lambda)$ in the longer wavelengths for increasing C_{SPM}, which avoids potential discontinuities in the derived C_{SPM}. More importantly, GAA_{SPM} does not require arbitrary

switching boundaries and is, therefore, more applicable for global waters than the hard-wired or blended switching schemes.

Although $R_{rs}(745)$ is most sensitive to C_{SPM} in the moderately turbid waters (see Fig. 3a), it appears that the weighted $R_{rs}(745)$ has insignificant contribution to GI_{SPM} for our datasets (see Fig. 8), which could probably be attributed to the fact that a relatively small number of moderately turbid samples were used in the algorithm calibration. Besides, we recalibrated the proposed algorithm without $R_{rs}(745)$ as an input, *i.e.*, a four-band algorithm. Although the performance of the four-band algorithm was only slightly worse than GAA_{SPM} for the entire range (the difference in rMAD is 0.4%), for the moderately turbid waters, rMAD of the derived C_{SPM} is 4.5% larger for the four-band algorithm than GAA_{SPM} (figure not shown here). Therefore, it is necessary to include $R_{rs}(745)$ in the development of a more inclusive dataset for the C_{SPM} algorithm to account for C_{SPM} retrieval in moderately turbid waters.

An overall rMAD of 41.3% for GAA_{SPM}-derived C_{SPM} still implies considerable uncertainties of GAA_{SPM} over the entire C_{SPM} range, which is mainly due to the relatively larger uncertainties of the derived C_{SPM} in less turbid waters. Note that rMADs of the derived C_{SPM} by all applicable algorithms in less turbid waters are mostly around 50%–60%, while rMADs of the retrieved C_{SPM} in highly turbid waters by most algorithms are only around 30%. This relatively poor $R_{rs}(\lambda)$-C_{SPM} relationship in less turbid waters could be explained by many factors. First, the uncertainties of measured $R_{rs}(671)$ in less turbid waters could be relatively large due to the very low values. Also, there might be inconsistency in measured $R_{rs}(\lambda)$ among the four *in situ* datasets, due to different instrumentations and correction methods to remove residual surface reflection for the above-water measurements. The uncertainties of measured C_{SPM} could also be relatively large for samples collected from less turbid waters, as fine particles (size $<$ 0.7 μm) were unlikely retained during the filtration due to the use of GF/F filter. On the other hand, in less turbid waters, the C_{SPM}-sensitive $R_{rs}(\lambda)$ shifts to shorter wavelengths, where the absorption coefficients of water components, such as phytoplankton, colored dissolved organic matter, and inorganic matter, have more impacts on the $R_{rs}(\lambda)$ variability. In other words, a change in the $R_{rs}(\lambda)$ spectrum in the visible domain is less likely the result of a change in C_{SPM} for such waters. Given that the component absorption coefficients could vary significantly among global oceans, the C_{SPM}-$R_{rs}(\lambda)$ in less turbid waters could be region-dependent. The present results confirm the weak correlation between C_{SPM} and $R_{rs}(\lambda)$ among global measurements (*e.g.*, small R^2 between C_{SPM} and $R_{rs}(\lambda)$ for C_{SPM} $<$ 10 mg/L in Fig. 3a). Nevertheless, compared to the listed algorithms in Section 2.3, the proposed GAA_{SPM} can partly account for the global variability of the $R_{rs}(\lambda)$-C_{SPM} relationship and yields the most accurate retrievals of C_{SPM} for relatively clear waters (Table 6).

For turbid waters, C_{SPM} is sensitive to $R_{rs}(\lambda)$ at longer wavelengths, where the particulate backscattering coefficient dominates the variability of $R_{rs}(\lambda)$ as water molecules are the main absorbing component. Thus, much higher R^2 values are found in the $R_{rs}(\lambda)$-C_{SPM} relationships in highly turbid waters (see Fig. 3a). As shown in Table 3, the recalibrated empirical constants are quite comparable with the original ones for the Doxaran_02 algorithm, given that the two sets of empirical constants were calibrated from different datasets. The rMAD of the derived C_{SPM} by Doxaran_02 using their original empirical constants equals to 36.9% (Table 5), while the recalibrated algorithm is slightly improved with rMAD of 31.6% (Table 6). Such findings confirm that a well-calibrated $R_{rs}(\lambda)$-C_{SPM} relationship from highly turbid waters has reduced regional variability, and therefore smaller errors are expected when applying it to very different regions. The reduced regional variability or data dependency of the $R_{rs}(\lambda)$-C_{SPM} relationship in highly turbid waters explains the consistent retrievals from the GAA_{SPM} and other algorithms that employ the $R_{rs}(862)$ in their algorithm's development, such as Dogliotti_15, Shen_10, and Doxaran_02.

Although Novoa_17, Dogliotti_15, Han_16, and Mao_12 also allow smooth retrievals for wide-range C_{SPM}, there are important differences between GAA_{SPM} and these algorithms. The Mao_12 is based on a rather complicated proxy and is therefore not easy to be implemented for satellite data, especially when the selected wavelengths for each index (Eq. (8) - (11)) require pre-calibrations and are data dependent. The large uncertainties of Novoa_17 (Fig. 4b) could be expected as Novoa_17 simply employs linear relationships between C_{SPM} and reflectance at the green and red bands to calculate the C_{SPM_Green} and C_{SPM_Red} (see Table 4), respectively, while such relationships are supposed to be region dependent (see Fig. 3a). Also, for Novoa_17, Dogliotti_15, and Han_16, they all employ switching boundaries in their algorithms, which could result in significant uncertainties for samples that were wrongly classified by the switching boundaries. Take Dogliotti_15 for example, in our *in situ* datasets, 19 samples with $\rho_w(671) > 0.07$ have C_{SPM} less than 50 mg/L. The switching scheme of Dogliotti_15 will employ $\rho_w(862)$ to derive C_{SPM} for these 19 samples and results in an rMAD of 187.1%. The wrong classification by the boundaries could partly explain why there are 'outliers' in the validation results of Novoa_17 (Fig. 4b), Dogliotti_15 (Fig. 4c), and Han_16 (Fig. 4d). The switch scheme of GAA_{SPM}, on the other hand, is based on the relative value of $R_{rs}(\lambda)$, instead of using a single band $R_{rs}(\lambda)$. Thus, GAA_{SPM} could effectively reduce the presence of such outliers. More importantly, the selected boundaries for relatively clear waters in Novoa_17, Dogliotti_15, and Han_16 were all from their respective study regions. However, the designated boundaries differed largely from $\rho_w(671) = 0.05$ to $\rho_w(671) = 0.094$, suggesting the saturation of $\rho_w(671)$ to the level of C_{SPM} could be region dependent (Shi and Wang, 2014). In this study, it appears that the boundary adopted in Dogliotti_15 works the best for our datasets, but such selection could fail for the calibration datasets in Novoa et al. (2017) and Han et al. (2016). Therefore, it is important to obtain a unified boundary for global applications for such type of algorithms. GAA_{SPM}, on the other hand, could be globally applicable, given that it does not require any hard switching boundaries.

4.2. Sensitivity of the derived C_{SPM} to uncertainties of R_{rs}(NIR)

Measured $R_{rs}(\lambda)$ at the NIR bands, by field instruments or satellite sensors, are always subject to uncertainties due to low signals in these wavelengths, especially for relatively clear waters. Validation of the NIR-SWIR atmospherically corrected $R_{rs}(\lambda)$ in Fig. 5 also shows that there might be relatively larger uncertainties of R_{rs}(NIR) from VIIRS-SNPP. Therefore, the sensitivity of the GAA_{SPM} to the uncertainties of R_{rs}(NIR) needs to be assessed, especially when the uncertainties of satellite-measured R_{rs}(NIR) could be high and are not well known. It should be noted that large uncertainties may also come from *in situ* R_{rs}(NIR) measurements, particularly for the relatively clear waters with very small R_{rs}(NIR) values.

Tests were carried out for the VIIRS-SNPP image used in Fig. 6 with systematic errors of ± 10% and ± 20% added to the two NIR bands at 745 and 862 nm, respectively. These error-included VIIRS-SNPP images were then employed to derive C_{SPM} using GAA_{SPM}. Fig. 9 shows the density scatter plots to present the comparisons between the originally derived C_{SPM} and the derived C_{SPM} from the error-included images. Statistical results are given for less turbid and highly turbid waters, respectively, to better demonstrate the impact of R_{rs}(NIR) uncertainties on the C_{SPM} retrieval for waters with different C_{SPM} ranges.

As shown in Fig. 9, uncertainties of R_{rs}(NIR) have negligible impacts on retrieved C_{SPM} for less turbid waters. A maximum of 20% error added to both $R_{rs}(745)$ and $R_{rs}(862)$ only results in less than 2% in the derived C_{SPM} for waters with C_{SPM} $<$ 50 mg/L, which is because $R_{rs}(671)$ is often 1–2 orders of magnitude larger than those of R_{rs}(NIR) in less turbid waters. Even with 40% error for the two NIR bands, $R_{rs}(671)$ still contributes the most weight to the GI_{SPM} for C_{SPM} $<$ 50 mg/L.

For turbid waters, the derived C_{SPM} is more sensitive to the uncertainties of R_{rs}(NIR), but overall has smaller or equivalent errors to

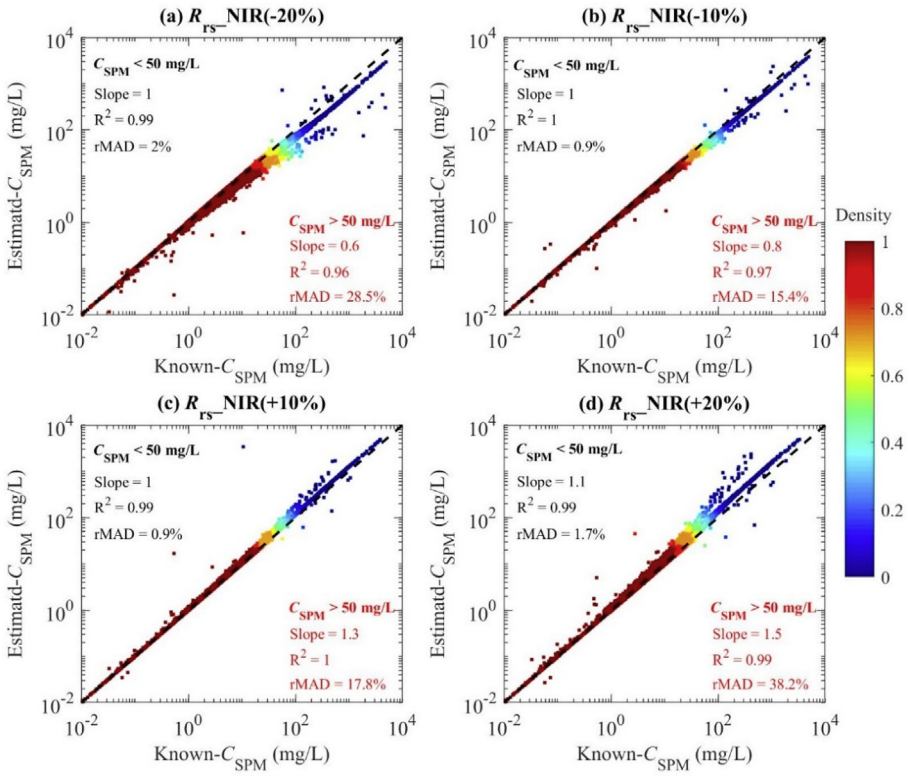

Fig. 9. Sensitivity analysis of GAA_{SPM} with respect to introduced error (± 10% and ± 20%) to $R_{rs}(\lambda)$ at two VIIRS NIR bands. The density scatters plots are based on the same VIIRS-SNPP image used in Fig. 6, with the known-C_{SPM} derived from the original VIIRS-SNPP data and the estimated-C_{SPM} derived from the error-included data.

the errors added to R_{rs}(NIR). As shown in Fig. 9a, a total of −40% error introduced to R_{rs}(745) and R_{rs}(862) results in an rMAD of 28.5% for the derived C_{SPM}, while a +40% error of R_{rs}(NIR) results in an rMAD of 38.2% for the derived C_{SPM}. In both cases, the errors of the derived C_{SPM} are smaller than the errors added to R_{rs}(NIR). Considering most atmospheric correction algorithms tend to underestimate R_{rs}(NIR), instead of the other way around, satellite-derived C_{SPM} by GAA_{SPM} is expected to be relatively noise-tolerant to the underestimation of R_{rs}(NIR) by the atmospheric correction.

5. Conclusions

In this study, we proposed an empirical algorithm that allows effective and seamless retrieval of C_{SPM} from ocean color across ocean to highly turbid river mouths, where existing algorithms in the literature will generally result in either unjustified numerical discontinuities or larger uncertainties. Validation of GAA_{SPM} and inter-comparison with existing algorithms (after recalibration with the datasets of this study) give confidence to the application of GAA_{SPM} over regions with a wide range of C_{SPM}. Given that the GAA_{SPM} is calibrated based on data collected from multiple estuarine and coastal regions around the world, GAA_{SPM} shows a feature of global applicability, which is essential to generate C_{SPM} maps from satellite ocean color sensors. Demonstrations using VIIRS-SNPP images over two turbid river mouths were presented, where GAA_{SPM} produced reasonable C_{SPM} maps in terms of both the range of the derived C_{SPM} and the spatial distribution pattern. Since there are many operational satellite ocean color sensors that have similar band configurations as VIIRS in the visible-NIR domains, GAA_{SPM} could be easily adapted to those satellite data after mild sensor-based adjustments to produce global C_{SPM} maps with improved spatial-temporal resolution through merging of multi-sensor data.

Declaration of competing interest

The authors declare that they have no known competing financial interests or personal relationships that could have appeared to influence the work reported in this paper.

Acknowledgment

This study was supported by the Joint Polar Satellite System (JPSS) funding for the NOAA ocean color calibration and validation (Cal/Val) project and the Outstanding Postdoctoral Scholarship of the State Key Laboratory of Marine Environmental Science at Xiamen University (Contribution No. 2019370). We thank Marcel Babin and Emmanuel Devred for providing the COASTLOOC dataset, and Els Knaeps and the co-authors of the SeaSWIR dataset for publishing this dataset. We thank Francis Gohin for providing the code of the Gohin_05 algorithm. Measurements from the Gulf of Mexico in the UMB dataset were funded by the NASA GEOCAPE project, and SPM concentrations were measured by Antonio Mannino (NASA/GFSC). The Changjiang dataset was provided by Fang Shen of East China Normal University. We would also like to express our sincere gratitude to all colleagues who contributed to the data collection and sharing. Finally, many thanks to NOAA Ocean Color Team and CoastWatch for providing the VIIRS-SNPP data. We also thank the four anonymous reviewers for their valuable comments. The views, opinions, and findings contained in this paper are those of the authors and should not be construed as an official NOAA or U.S. Government position, policy, or decision.

Appendix A. Supplementary data

Supplementary data to this article can be found online at https://doi.org/10.1016/j.rse.2019.111491.

Appendix 1. Interpolation of the measured $R_{rs}(\lambda)$ for the COASTLOOC dataset

Absorption by pure water dominates the total absorption coefficients at NIR bands in offshore waters and open oceans. To obtain accurate $R_{rs}(\lambda)$ at 745 nm and construct a reasonable spectral feature at the NIR bands for the COASTLOOC dataset from the measured $R_{rs}(\lambda)$ at the twelve wavelengths (see Table 1), a semi-analytical interpolation approach is employed.

Non-water absorption and backscattering coefficients (a_{nw} and b_{bp}, in m^{-1}) are first derived from measured $R_{rs}(\lambda)$ at the twelve COASTLOOC wavelengths using the quasi-analytical algorithm (QAA) (Lee et al., 2002). The derived a_{nw} is then linearly interpolated to hyperspectral data from 411 to 866 nm with an increment of 1 nm. The derived b_{bp} is interpolated to the same wavelength range following the parameterization of b_{bp} in QAA. Given that absorption and backscattering coefficients of pure water (a_w and b_{bw}) are known (Kou et al., 1993; Morel, 1974; Pope and Fry, 1997), hyperspectral total absorption and backscattering coefficients ($a(\lambda)$ and $b_b(\lambda)$) are estimated by,

$$a(\lambda) = a_{nw}(\lambda) + a_w(\lambda) \tag{A1}$$

$$b_b(\lambda) = b_{bp}(\lambda) + b_{bw}(\lambda) \tag{A2}$$

Hyperspectral $R_{rs}(\lambda)$ can be finally determined from $a(\lambda)$ and $b_b(\lambda)$ following,

$$r_{rs}(\lambda) = g_0\left(\frac{b_b}{b_b + a}\right) + g_1\left(\frac{b_b}{b_b + a}\right)^2 \tag{A3}$$

$$R_{rs}(\lambda) = 0.52 r_{rs}(\lambda)/(1 - 1.7 r_{rs}(\lambda)) \tag{A4}$$

where $r_{rs}(\lambda)$ is the remote sensing reflectance beneath the surface with $g_0 = 0.089$ and $g_1 = 0.125$ (Gordon et al., 1988; Lee et al., 1999).

Using QAA for the retrieval of a_{nw} and b_{bp}, instead of inversion algorithms using spectral optimization, would ensure the interpolated $R_{rs}(\lambda)$ matches the measured $R_{rs}(\lambda)$ exactly at the twelve COASTLOOC wavelengths. To evaluate the performance of the semi-analytical interpolation approach, measured $R_{rs}(\lambda)$ of the UMB dataset was first resampled to the twelve COASTLOOC wavelengths, and $R_{rs}(745)$ was then estimated from the above described semi-analytical interpolation, as well as from the linear interpolation between $R_{rs}(705)$ and $R_{rs}(779)$. Fig. A1 shows a comparison of estimated $R_{rs}(745)$ by the two interpolation methods, which demonstrates that the semi-analytical approach can provide much more consistent estimations of $R_{rs}(745)$ than the linear interpolation method.

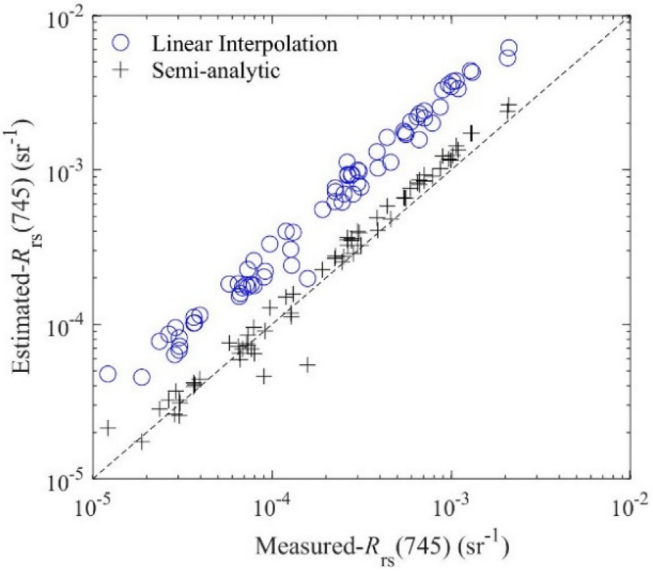

Fig. A1. Evaluation of the interpolated $R_{rs}(\lambda)$ at 745 nm by the linear and the semi-analytic approaches, using the UMB dataset as an example.

References

Austin, R.W., 1974. Inherent spectral radiance signatures of the ocean surface, p. 2.1–2.20. In: Ocean Color Analysis. Scripps Institution of Oceanography, San Diego, CA.

Babin, M., Stramski, D., Ferrari, G.M., Claustre, H., Bricaud, A., Obolensky, G., Hoepffner, N., 2003. Variations in the light absorption coefficients of phytoplankton, nonalgal particles, and dissolved organic matter in coastal waters around Europe. J. Geophys. Res. Oceans 108, 3211.

Binding, C., Bowers, D., Mitchelson-Jacob, E., 2005. Estimating suspended sediment concentrations from ocean colour measurements in moderately turbid waters; the impact of variable particle scattering properties. Remote Sens. Environ. 94, 373–383.

D'Sa, E.J., Miller, R.L., McKee, B.A., 2007. Suspended particulate matter dynamics in coastal waters from ocean color: application to the northern Gulf of Mexico. Geophys. Res. Lett. 34, L23611.

Dogliotti, A., Ruddick, K.G., Nechad, B., Doxaran, D., Knaeps, E., 2015. A single algorithm to retrieve turbidity from remotely-sensed data in all coastal and estuarine waters. Remote Sens. Environ. 156, 157–168.

Doxaran, D., Cherukuru, N., Lavender, S.J., 2006. Apparent and inherent optical properties of turbid estuarine waters: measurements, empirical quantification relationships, and modeling. Appl. Opt. 45, 2310–2324.

Doxaran, D., Froidefond, J.-M., Lavender, S., Castaing, P., 2002a. Spectral signature of highly turbid waters: application with SPOT data to quantify suspended particulate matter concentrations. Remote Sens. Environ. 81, 149–161.

Doxaran, D., Froidefond, J.M., Castaing, P., 2002b. A reflectance band ratio used to estimate suspended matter concentrations in sediment-dominated coastal waters. Int. J. Remote Sens. 23, 5079–5085.

Doxaran, D., Froidefond, J.M., Castaing, P., 2003. Remote-sensing reflectance of turbid sediment-dominated waters. Reduction of sediment type variations and changing illumination conditions effects by use of reflectance ratios. Appl. Opt. 42, 2623–2634.

Fargion, G.S., Mueller, J.L., 2000. Ocean Optics Protocols for Satellite Ocean Color Sensor Validation, Revision 2. National Aeronautics and Space Administration, Goddard Space Flight Center.

Gohin, F., Druon, J., Lampert, L., 2002. A five channel chlorophyll concentration algorithm applied to SeaWiFS data processed by SeaDAS in coastal waters. Int. J. Remote Sens. 23, 1639–1661.

Gohin, F., Loyer, S., Lunven, M., Labry, C., Froidefond, J.-M., Delmas, D., Huret, M.,

Herbland, A., 2005. Satellite-derived parameters for biological modelling in coastal waters: illustration over the eastern continental shelf of the Bay of Biscay. Remote Sens. Environ. 95, 29–46.
Gordon, H.R., Brown, O.B., Evans, R.H., Brown, J.W., Smith, R.C., Baker, K.S., Clark, D.K., 1988. A semianalytic radiance model of Ocean color. J. Geophys. Res. Atmos. 93, 10909–10924.
Gordon, H.R., Wang, M., 1994. Retrieval of water-leaving radiance and aerosol optical thickness over the oceans with SeaWiFS: a preliminary algorithm. Appl. Opt. 33, 443–452.
Han, B., Loisel, H., Vantrepotte, V., Mériaux, X., Bryère, P., Ouillon, S., Dessailly, D., Xing, Q., Zhu, J., 2016. Development of a Semi-Analytical Algorithm for the Retrieval of Suspended Particulate Matter from Remote Sensing over Clear to Very Turbid Waters. Remote Sens. 8, 211.
He, X., Bai, Y., Pan, D., Huang, N., Dong, X., Chen, J., Chen, C.-T.A., Cui, Q., 2013. Using geostationary satellite ocean color data to map the diurnal dynamics of suspended particulate matter in coastal waters. Remote Sens. Environ. 133, 225–239.
IOCCG, 2000. Remote sensing of Ocean colour in coastal, and other optically-complex, waters. In: Sathyendranath, S. (Ed.), Reports Of the International Ocean-Colour Coordinating Group. IOCCG, Dartmouth, Canada No.3.
IOCCG, 2006. Remote sensing of inherent optical properties: fundamentals,Tests of algorithms, and applications. In: Lee, Z.P. (Ed.), Reports Of the International Ocean-Colour Coordinating Group. IOCCG, Dartmouth, Canada No. 5.
Jiang, L., Wang, M., 2014. Improved near-infrared ocean reflectance correction algorithm for satellite ocean color data processing. Opt. Express 22, 21657–21678.
Knaeps, E., Doxaran, D., Dogliotti, A., Nechad, B., Ruddick, K., Raymaekers, D., Sterckx, S., 2018. The SeaSWIR dataset. Earth Syst. Sci. Data 10, 1439–1449.
Knaeps, E., Ruddick, K., Doxaran, D., Dogliotti, A., Nechad, B., Raymaekers, D., Sterckx, S., 2015. A SWIR based algorithm to retrieve total suspended matter in extremely turbid waters. Remote Sens. Environ. 168, 66–79.
Kou, L., Labrie, D., Chylek, P., 1993. Refractive indices of water and ice in the 0.65-to 2.5-μm spectral range. Appl. Opt. 32, 3531–3540.
Laws, E.A., 1997. Mathematical Methods for Oceanographers: an Introduction. John Wiley & Sons.
Lee, Z., Carder, K.L., Mobley, C.D., Steward, R.G., Patch, J.S., 1999. Hyperspectral remote sensing for shallow waters. 2. Deriving bottom depths and water properties by optimization. Appl. Opt. 38, 3831–3843.
Lee, Z., Pahlevan, N., Ahn, Y.-H., Greb, S., O'Donnell, D., 2013. Robust approach to directly measuring water-leaving radiance in the field. Appl. Opt. 52, 1693–1701.
Lee, Z.P., Carder, K.L., Arnone, R.A., 2002. Deriving inherent optical properties from water color: a multiband quasi-analytical algorithm for optically deep waters. Appl. Opt. 41, 5755–5772.
Loisel, H., Mangin, A., Vantrepotte, V., Dessailly, D., Dinh, D.N., Garnesson, P., Ouillon, S., Lefebvre, J.-P., Mériaux, X., Phan, T.M., 2014. Variability of suspended particulate matter concentration in coastal waters under the Mekong's influence from ocean color (MERIS) remote sensing over the last decade. Remote Sens. Environ. 150, 218–230.
Loisel, H., Morel, A., 2001. Non-isotropy of the upward radiance field in typical coastal (Case 2) waters. Int. J. Remote Sens. 22, 275–295.
Luo, Y., Doxaran, D., Ruddick, K., Shen, F., Gentili, B., Yan, L., Huang, H., 2018. Saturation of water reflectance in extremely turbid media based on field measurements, satellite data and bio-optical modelling. Opt. Express 26, 10435–10451.
Mao, Z., Chen, J., Pan, D., Tao, B., Zhu, Q., 2012. A regional remote sensing algorithm for total suspended matter in the East China Sea. Remote Sens. Environ. 124, 819–831.
Min, J., Choi, J., Park, Y., Ryu, J., 2013. Retrieval of suspended sediment concentration in the coastal waters of yellow sea from Geostationary Ocean color imager (GOCI). In: Proc. Of International Symposium on Remote Sensing, pp. 809–912.
Mobley, C.D., 1999. Estimation of the remote-sensing reflectance from above-surface measurements. Appl. Opt. 38, 7442–7455.
Morel, A., 1974. Optical properties of pure water and pure sea water. Opt. Asp. Oceanogr. 1–24.
Nechad, B., Ruddick, K., Park, Y., 2010. Calibration and validation of a generic multisensor algorithm for mapping of total suspended matter in turbid waters. Remote Sens. Environ. 114, 854–866.
Novoa, S., Doxaran, D., Ody, A., Vanhellemont, Q., Lafon, V., Lubac, B., Gernez, P., 2017. Atmospheric corrections and multi-conditional algorithm for multi-sensor remote sensing of suspended particulate matter in low-to-high turbidity levels coastal waters. Remote Sens. 9, 61.
Pope, R.M., Fry, E.S., 1997. Absorption spectrum (380 –700 nm)of pure water. II. Integrating cavity measurements. Appl. Opt. 36, 8710–8723.
Ruddick, K.G., De Cauwer, V., Park, Y.-J., Moore, G., 2006. Seaborne measurements of near infrared water-leaving reflectance: the similarity spectrum for turbid waters. Limnol. Oceanogr. 51, 1167–1179.
Seegers, B.N., Stumpf, R.P., Schaeffer, B.A., Loftin, K.A., Werdell, P.J., 2018. Performance metrics for the assessment of satellite data products: an ocean color case study. Opt. Express 26, 7404–7422.
Shang, Z., Lee, Z., Dong, Q., Wei, J., 2017. Self-shading associated with a skylight-blocked approach system for the measurement of water-leaving radiance and its correction. Appl. Opt. 56, 7033–7040.
Shen, F., Salama, M.S., Zhou, Y.X., Li, J.F., Su, Z.B., Kuang, D.B., 2010a. Remote-sensing reflectance characteristics of highly turbid estuarine waters - a comparative experiment of the Yangtze River and the Yellow River. Int. J. Remote Sens. 31, 2639–2654.
Shen, F., Verhoef, W., Zhou, Y.X., Salama, M.S., Liu, X.L., 2010b. Satellite estimates of wide-range suspended sediment concentrations in Changjiang (yangtze) estuary using MERIS data. Estuar. Coasts 33, 1420–1429.
Shen, F., Zhou, Y.X., Li, J.F., He, Q., Verhoef, W., 2013. Remotely sensed variability of the suspended sediment concentration and its response to decreased river discharge in the Yangtze estuary and adjacent coast. Cont. Shelf Res. 69, 52–61.
Shen, F., Zhou, Y.X., Peng, X.Y., Chen, Y.L., 2014. Satellite multi-sensor mapping of suspended particulate matter in turbid estuarine and coastal ocean, China. Int. J. Remote Sens. 35, 4173–4192.
Shi, W., Wang, M., 2014. Ocean reflectance spectra at the red, near-infrared, and shortwave infrared from highly turbid waters: a study in the Bohai Sea, Yellow Sea, and East China Sea. Limnol. Oceanogr. 59, 427–444.
Shi, W., Wang, M., 2007. Detection of turbid waters and absorbing aerosols for the MODIS ocean color data processing. Remote Sens. Environ. 110, 149–161.
Shi, W., Zhang, Y., Wang, M., 2018. Deriving total suspended matter concentration from the near-infrared-based inherent optical properties over turbid waters: a case study in lake taihu. Remote Sens. 10, 333.
Siswanto, E., Tang, J., Yamaguchi, H., Ahn, Y.-H., Ishizaka, J., Yoo, S., Kim, S.-W., Kiyomoto, Y., Yamada, K., Chiang, C., 2011. Empirical ocean-color algorithms to retrieve chlorophyll-a, total suspended matter, and colored dissolved organic matter absorption coefficient in the Yellow and East China Seas. J. Oceanogr. 67, 627.
Volpe, V., Silvestri, S., Marani, M., 2011. Remote sensing retrieval of suspended sediment concentration in shallow waters. Remote Sens. Environ. 115, 44–54.
Wang, M., 2007. Remote sensing of the ocean contributions from ultraviolet to near-infrared using the shortwave infrared bands: simulations. Appl. Opt. 46, 1535–1547.
Wang, M., Shi, W., 2007. The NIR-SWIR combined atmospheric correction approach for MODIS ocean color data processing. Opt. Express 15, 15722–15733.
Wang, M., Shi, W., Tang, J., 2011. Water property monitoring and assessment for China's inland Lake Taihu from MODIS-Aqua measurements. Remote Sens. Environ. 115, 841–854.
Wang, M., Tang, J., Shi, W., 2007. MODIS-derived ocean color products along the China east coastal region. Geophys. Res. Lett. 34.
Zhang, M., Tang, J., Dong, Q., Song, Q., Ding, J., 2010. Retrieval of total suspended matter concentration in the Yellow and East China Seas from MODIS imagery. Remote Sens. Environ. 114, 392–403.
Zhang, T., Fell, F., 2007. An empirical algorithm for determining the diffuse attenuation coefficient K-d in clear and turbid waters from spectral remote sensing reflectance. Limnol Oceanogr. Methods 5, 457–462.